UNIVERSITY OF CALIFORNIA, SAN DIEGO

Experimental Studies of Thermal Fluctuations in Electron Plasmas

A dissertation submitted in partial satisfaction of the
requirements for the degree Doctor of Philosophy
in
Physics

by

Nobuyasu Shiga

Committee in charge:

Professor C. Fred Driscoll, Chair
Professor Daniel H. E. Dubin
Professor Roy W. Gould
Professor Kevin B. Quest
Professor Clifford M. Surko
Professor George Tynan

2004

The dissertation of Nobuyasu Shiga is approved, and it is acceptable in quality and form for publication on microfilm:

Chair

University of California, San Diego

2004

TABLE OF CONTENTS

LIST OF FIGURES

ABSTRACT OF THE DISSERTATION

Experimental Studies of Thermal Fluctuations in Electron Plasmas

by

Nobuyasu Shiga
Doctor of Philosophy in Physics
University of California, San Diego, 2003
Professor C. Fred Driscoll, Chair

We have detected the thermally excited charge fluctuations in pure electron plasmas over a temperature range of $0.05 < \mathrm{k_B}T < 10\mathrm{eV}$. These fluctuation spectra have both a global mode component and a random particle fluctuation component. At low temperatures, the $m_\theta = 0,\ k_z = 1, 2, 3, \ldots$ Trivelpiece-Gould modes are weakly damped and dominate, since the random particle component is suppressed by Debye-shielding. As the temperature increases, the broad random particle component increases in between the modes.

We have developed 3 different non-perturbative methods to determine the plasma temperature. These 3 methods are valid in different regimes depending on the Debye length normalized by the plasma radius $\frac{\lambda_D}{R_p}$, and on the plasma length normalized by the plasma radius $\frac{L_p}{R_p}$.

The first method focuses on the near-Lorentzian spectrum of thermal fluctuations near a weakly damped mode. Each weakly damped mode has the same

energy as the electron temperature. The measured emission spectrum together with a plasma-antenna impedance calibration uniquely determines the temperature of the plasma, using Nyquist theorem. Experimentally this method gives the correct temperature, agreeing with the standard “dump” temperature measurements when $\frac{\lambda_D}{R_p} < 0.3$.

The second method utilizes the emission spectrum over a broad frequency range encompassing several modes and the non-resonant fluctuations between modes. The Nyquist theorem together with a kinetic theory calculation of the plasma-antenna impedance determines the temperature from the broad fluctuation spectrum. Kinetic theory implicitly assumes that Landau damping is the only damping mechanism, and also assumes an infinite length for the plasma. This method works if $\frac{\lambda_D}{R_p} > 0.2$ so that Landau damping is dominant, and if $\frac{L_p}{R_p} > 20$ so that finite-length corrections to Landau damping are negligible.

The third method utilizes the total (frequency-integrated) number δN of the fluctuating image charges on the antenna, and comparison with the thermodynamic calculation determines the plasma temperature. This method works when $\frac{\lambda_D}{R_p} > 0.2$ so that the plasma and load impedances satisfy $|Z_p| \gg |Z_\ell|$; but one need to separately determine the plasma density n, L_p, and R_p to calculate the expected $\delta N(T)$.

1

Introduction

Non-neutral plasmas are unique in that they can be trapped in a rotating near-thermal-equilibrium state by static electric and magnetic fields. Steady-state confinement of $N = 10^3 - 10^9$ electrons, ions, or anti-matter particles [1, 18, 22] is routinely used in plasma experiments, atomic physics [41], and spectroscopy [31]. The thermal equilibrium characteristics become most evident with the formation of Coulomb crystals [33] when pure ion plasmas are cooled to the liquid and solid regimes at sub-Kelvin temperatures, but the higher temperature plasma regime studied here is also well-described by near-equilibrium statistical mechanics [37]. These stable near-thermal-equilibrium plasmas exhibit fluctuating electric fields, which are excited and damped by the random motions of the particles.

In the high temperature limit , this fluctuation is a random motion of electrons with no interaction to each other, as is the case for the ideal gas. Therefore, the density fluctuation spectrum reflects the thermal velocity distribution of the plasma, which is a Gaussian with width $\sim v_{th}/L_p$. Preliminary work by the Group at Brigham Young University [34] focused on the fluctuation spectrum in-between-modes, neglected the interactions between particles.

As the temperature decreases from this high temperature limit, Debye shielding suppress the random motion of particles, and the collective effects (i.e. waves) become dominant. These weakly damped plasma waves may be considered to be the normal modes of the system; in traps with finite length and radius, these modes appear at discrete Trivelpiece-Gould (T-G) standing mode frequencies [38, 43]. In an isolated equilibrium plasma, each standing mode would have an average electrostatic potential energy of $\frac{1}{2}\mathrm{k_B}T$ per mode; here, the mode coupling to the receiver electronics can be comparable to the coupling to the (rotating) thermal equilibrium plasma, complicating the picture slightly.

Somewhat simpler center-of-mass "trap modes" are commonly observed in the single-particle regime with highly tuned resonant circuits in hyperbolic traps [44], diagnosing the number of particles, but not their temperature. At higher frequencies, thermal excitation of cyclotron modes are readily observed in warm non-neutral [20] and hot fusion plasmas [15]; upper hybrid modes have also been used as a thermal diagnostic [40]. Temperature information can also be obtained by measuring changes in the frequencies of particular modes; this is in some sense a simpler version of the methods developed here [2]. In space plasmas, thermal noise diagnostics [32] are substantially different because of the lack of boundaries. In the crystallized regime, equipartition of mode energy has been observed in dusty plasmas [35]. In mirrors of a laser resonator [19], thermally excited vibrations are carefully analyzed assuming that each mode has energy $\mathrm{k_B}T$.

Historically, the ionospheric microwave back-scattering observations in the 1960s were the first observations of the fluctuation spectrum in plasmas [4]. The scattering is due to the electrons that are "bound" to ions, and therefore the spectrum of the backscattering around the incident wave frequency reflects the ion motion, instead of the electron motion. The observed spectrum revealed the strongly damped ion-acoustic wave on top of a Gaussian ion velocity distribution [14]. Theory calculations predicted that as the ratio of electron temperature and ion temperature T_e/T_i increases, the ion-acoustic waves become more prominent due to decreased damping. This transition was not observed experimentally because it is difficult to change the temperature of the ionosphere. On the other hand, in our laboratory plasma, the analogous transition was observed as we changed the temperature of the electron plasma.

In this thesis, we present observations of thermally excited fluctuations in pure electron plasmas over a temperature range of $0.05 < \mathrm{k_B} T_p < 10eV$, using a room temperature (0.03eV) receiver. At high temperature (λ_D / R_p >0.3), the spectrum is a broad Gaussian that reflects velocity distribution of the electrons, with heavily damped modes visible in addition. As the temperature decreases, the broad Gaussian spectrum decreases in amplitude due to Debye-shielding; and instead, the mode peaks rises up because Landau damping decreases exponentially as the temperature decreases.

We have developed three different non-pertubative strategies to determine the plasma temperature. The first method focus on the spectrum near a mode. Each weakly damped mode spectrum is nominally a Lorentzian at frequency ω_m with half-width γ_m, superimposed on the receiver-generated noise modified by plasma absorption. By Nyquist's theorem, the thermal noise driving a mode is proportional to $\mathrm{k_B} T_p$ and proportional to the real part of the mode/antenna impedance Z_m [20]. The impedance Z_m can be obtained directly from the received spectra when the receiver impedance and noise-temperature T_ℓ are significant; or it can be calculated from a kinetic theory of random test particles incorporating the plasma dielectric. The impedance Z_m represents the impedance of the plasma $Z_p(\omega)$ near the mode at ω_m. The dissipation of Z_m represents the mode damping γ_m, coupled to the receiver by a "geometric" capacitance $\mathcal{G}$. This diagnostic determines $T_p, T_\ell, \omega_m, \gamma_m$ and $\mathcal{G}$.

The second method requires the emission spectrum over a broad frequency range spanning several modes in order to compare to the kinetic theory calculation. Unfortunately, Kinetic theory implicitly assumes that Landau damping is the only damping mechanism and neglects all geometrical end effects. This theory matches the measured spectra extremely well if the temperature is large enough that Landau damping is dominant and if the plasma is long compared to the radius. Outside these regimes, the theory limitation become apparent. This diagnostic determines

4 plasma parameters T_p, n_0, k_z, R_p. The mode characteristics ω_m, γ_m and $\mathcal{G}$ then follow from theory.

The third method requires only the total (frequency-integrated) number fluctuation δN, and comparison with a thermodynamic calculation determines the plasma temperature. This theory does not assume the form of damping, but one needs to determine n, L_p, R_p separately to calculate the fluctuation $\delta N(T)$ for comparison to the measured δN.

As long as a mode of interest is weakly damped, the first method is robust, and a single emission spectrum determines the temperature with moderate accuracy (± 20%). This method does not assume the form of the damping; but it does assume that the mode is in "equilibrium" with the plasma, i.e. not being excited by external effects. This method can readily obtain the plasma temperature 100 times per second, given only a passive antenna signal. When the temperature is high enough that the mode spectrum deviates from a Lorentzian, one can use kinetic theory calculation if the plasma is long enough that finite-length corrections to Landau damping are negligible. Finally, one can use the thermodynamics to calculate the total fluctuation for plasmas with $\frac{\lambda_D}{R_p} > 0.2$ so that $|Z_p| \gg |Z_\ell|$. This thermodynamic calculation has no assumption of the damping but requires the separate determination of n_0, L_p, R_p.

2

Experimental Apparatus

Fluctuation measurements were obtained from pure electron plasmas contained in two similar Penning-Malmberg traps ("IV" and "EV") shown schematically in Figure 2.1. These two traps differ mainly in plasma diameter and magnetic field strength. The IV trap consists of a series of hollow conducting cylinders of radius $R_w = 2.86$ cm contained in ultra-high vacuum at $P \approx 10^{-10}$ Torr with a uniform axial magnetic field of $B_z = 30$ kG. Electrons are injected from a hot tungsten filament, and contained axially by voltages $V_{\text{conf}} \approx -200$ V on end electrodes. Typical plasmas have $N \approx 10^9$ electrons in a column length $L_p \approx 41$ cm, with a plasma radius $R_p \approx 0.2$ cm and a central density $n_0 \approx 10^7$ cm^{-3}. (For EV, the parameters are $B_z = 0.375$ kG, $R_p = 1.7$ cm, $R_w = 3.8$ cm, and $L_p = 15 \sim 37$ cm.)

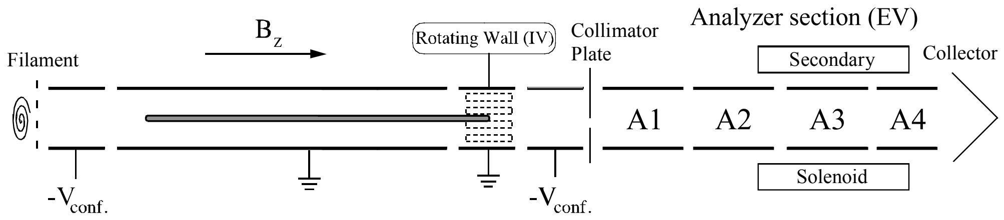

Figure 2.1: Schematic diagram of a cylindrical Penning-Malmberg trap.

The plasma density profile $n(r)$ and the temperature T_p are obtained by dumping the plasma axially and measuring the total charge passing through a hole in a scanning collimator plate. Both measurements require shot-to-shot reproducibility of the injected plasma, and we typically observe variability $\delta n/n \leq 1\%$. On IV, a weak "rotating wall" perturbation at $f_{\mathrm{RW}} \sim 0.5$ MHz is used to obtain steady-state confinement of the electron column. [3, 26] The EV plasmas expand radially towards the wall with a characteristic "mobility" time of $\tau_m \approx 100$ sec, so the electrons are repetitively injected and dumped. The spectrum analyzer scans analyzed here typically require about 0.5 sec to complete and 10 msec for transient digitizer.

To control the temperature, we apply auxiliary "wiggle" heating by modulating one electrode voltage at a frequency $f_h = 0.8 - 1.0$ MHz, where f_h is adjusted so that all harmonics are distinct from the T-G mode of interest. On the EV apparatus, a "heating burst" is applied before the measurement; on the IV apparatus, the heating is applied continuously to balance the cooling due to the cyclotron radiation.

2.1 Temperature Diagnostics

Destructive temperature diagnostic are commonly used to obtain the parallel and perpendicular temperatures $T_{\|}$ and $T_{\perp}(r)$; this thesis develops non-destructive (passive) methods. For simplicity, we generally express temperatures in energy units, eliminating the constant $\mathrm{k_B}$. That is, $\mathrm{k_B}T$ and T will be used interchangeably, with $\mathrm{k_B}$ written in CGS formulas.

2.1.1 Perpendicular Temperature

The $T_{\perp}$ diagnostic on the EV apparatus operates by measuring the change in the parallel energy of the dumped electron when a secondary magnetic field causes some perpendicular energy to be transformed to the parallel direction. This is commonly called a 'magnetic beach' analyzer [27]. After the end gate has been lowered, the plasma expands ('disassembles') towards the collimator. During this disassembly, the plasma electrostatic energy increases the parallel velocities in a complicated fashion. However, since the time for a gyro orbit ($\sim$1 nsec) is small compared to the disassembly time ($\sim$1 μsec), the gyromagnetic moment $\mu = mv_\perp^2/2B$ is conserved, and the collimated beam that passes through the hole enters the analyzer region with its perpendicular energy distribution unchanged.

The collimated beam then encounters a potential barrier caused by the secondary magnetic field B_s of the analyzer solenoid. Since the space charge of the diffuse beam is small, each electron conserves its total kinetic energy $\mathcal{H}_\perp + \mathcal{H}_\| = \frac{1}{2}(v_\perp^2 + v_\|^2)$ as well as the gyromagnetic moment. In order to conserve both quantities, the average parallel energy must change by $\delta\mathcal{H}_\| = -(B_s/B_z)\mathrm{k_B}T_\perp$ within the analyzer solenoid. This change in parallel energy is measured by applying retarding voltages to the analyzer electrodes. If an electron's $v_\|$ drops low enough, it will not make it through cylinder A3. By measuring the density collected at the end as a function of the voltage on A3, and repeating with different B_s values, the perpendicular energy distribution was constructed to $\sim$ 15% accuracy.

2.1.2 Parallel Temperature

In IV, the parallel temperature $T_\|(r = 0)$ is measured only at the radial center using an "evaporative" technique [13]. For this measurement, the dump voltage is slowly ramped to ground over a time ($\sim$10 ms) which is long compared to the dump time for a density measurement ($\sim 1\mu$s). During the slow ramp of the confinement potential, electrons with sufficient parallel energy escape the confinement region, and are collected by the end plate. The number of collected electrons vs ramped voltage is digitized and fit to the tail of a Maxwellian distribution, which defines $T_\|$. Since the space charge potential is most negative at the center of the plasma, the electrons escape from there first. The diagnostic thus measures the temperature parallel to the magnetic field at the axial center of the plasma $T_\|(0)$. In practice, we take the average value of the temperature for 3 shots, with a shot-to-shot deviation in the calculation that is typically $\delta T/T \approx 0.2$.

2.1.3 Equilibration Rates

The rate at which electrons get thermalized along any single field line is much larger than the cross-field transport rates required for "global" thermal equilibrium. We will consider this local thermalization rate first.

Electrons thermalize along the magnetic field lines due to collisions with other electrons. The electron-electron collision frequency for 90° scattering collisions is given by

$$\begin{aligned}\nu_{ee} &\equiv \frac{16\sqrt{\pi}}{15} n\, \bar{v}\, b^2\ \ln(r_c/b) \\ &\approx 180\mathrm{sec}^{-1}\left[\frac{n_p}{10^7\mathrm{cm}^{-3}}\right]\left[\frac{1\mathrm{eV}}{T_p}\right]^{3/2} \ln\left\{\left(\frac{B}{380G}\right)^{-1}\left(\frac{\mathrm{k_B}T}{1\mathrm{eV}}\right)^{3/2}\right\}\end{aligned} \tag{2.1}$$

Here, $r_c \equiv \bar{v}/\Omega_c$ is the cyclotron radius and $b \equiv e^2/\mathrm{k_B}T$ is the distance of closest approach for thermal elections. At the magnetic field in IV, $B = 30,000$ Gauss, the numerical factor in Eq. (2.1) decreases from 180 to 104.

The rate at which the parallel and perpendicular degrees of freedom come into equilibrium with each other is accurately described by the rate predicted from "classical" short-range collisions [28], as

$$\nu_{\perp\parallel} \equiv \frac{3}{2}\nu_{ee}. \tag{2.2}$$

In the following chapters, we make no distinction between the perpendicular temperature, $T_\perp$, and the parallel temperature, $T_\parallel$. In essence, we assume that these degrees of freedom are in equilibrium with each other.

In practice, we also ignore radial variations in the temperature, and describe the plasma with one value of T_p. In EV, T_p is found by taking an error-weighted average of the measured (nearly uniform) values of $T_\perp(r)$ across the diameter of the plasma. In IV, the temperature is only measured at $r = 0$, and here we use $T_p = T_\parallel(0)$. We can experimentally verify that the variations are typically small in EV, as shown in Figure 2.2, but I must *assume* that they are also small in IV.

There are theoretical reasons why the temperature should be relatively uniform. The heat conduction theory of Dubin and O'Neil predicts relatively rapid transport of heat across magnetic field lines [11], and these predictions have been recently verified with experiments on pure-ion plasmas by Hollmann and Anderegg [24, 25].

2.2 Global and Local Thermal Equilibrium

Non-neutral plasmas are unique in that they relax to a state of "global" thermal equilibrium [12,37]. This global equilibrium state is characterized by a uniform temperature T_{eq}, a uniform fluid rotation frequency ω_{eq}, and a nearly uniform density characterized by the central density n_{eq}. The three parameters($T_{eq},\ \omega_{eq},\ n_{eq}$) are themselves uniquely determined by the total number of particles N_{tot}, the total energy H, and the total angular momentum P_θ of the plasma [7, 39, 42]

Experiments have characterized the relaxation of a markedly non-equilibrium initial plasma, e.g. a "hollow" density profile [8]. On the collisional time scale($1/\nu_{ee} \sim$ 1 - 10ms) thermal equilibrium is quickly established axially along each field line (local thermal equilibrium). Due to the azimuthal rotation and assumed θ-symmetry, the plasma can be thought of as being composed of cylindrical shells. Each individual shell is itself in equilibrium, but different shells are not in equilibrium with each other. On a longer time scale, the plasma evolves to a global thermal equilibrium state due to transport of heat and particles across the magnetic field. For the plasmas studied, the time to come to global thermal equilibrium was found to be on the order of $\tau_{eq} \sim$ 1-10 sec. We have performed fluctuation measurement in both global and local equilibrium plasmas. In IV plasmas, measurements were performed 100 sec after the injection, so the plasma had fully equilibrated. In EV plasmas, measurements were performed 0.5 sec after the injection, so we typically made the initial condition with a near-equilibrium profile $n(r)$.

Typical density $n(r)$ and $T_\perp(r)$ profiles for EV plasma are shown in Fig. 2.2.

This data was taken with the EV machine, with parameters $p = 10^{-10}$ Torr,

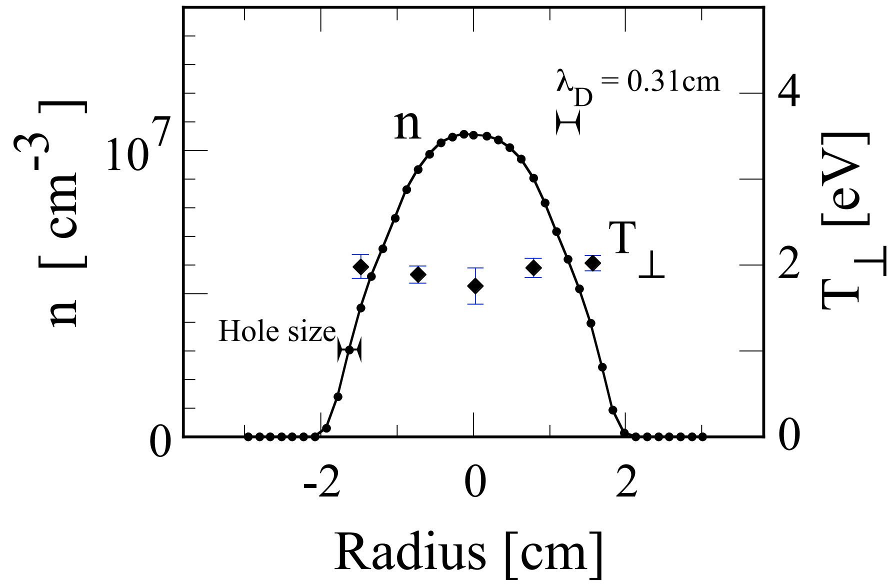

Figure 2.2: Typical Radial Profile of Density (circles) and Temperature (diamonds) for an EV plasma

B_z=380 Gauss, $n_0 = 1.1 \times 10^7 \text{cm}^{-3}$, having a confinement length L_p=27.73 cm, having a collimator hole diameter= 0.32 cm. The density $n(r)$ at each radius was averaged over 4 shots, and the perpendicular temperature $T_\perp$ was obtained as a result of about 80 shots at each radius. The Debye length λ_D is defined as

$$\lambda_D \equiv \sqrt{\frac{\mathrm{k_B} T_p}{4\pi e^2 n_0}} = 0.235\text{cm} \ \left[\frac{T_p}{1eV}\right]^{1/2} \left[\frac{10^7\text{cm}^{-3}}{n_0}\right]^{1/2} . \tag{2.3}$$

The temperature is flat over radius even though the density is not yet constant over radius, because the heat transport across the magnetic field is much faster than the particle transport [24].

3

Temperature Diagnostic using a Weakly Damped Mode

When the temperature T_p of the plasma is low such that $\lambda_D/R_p < 0.3$, weakly-damped standing mode fluctuations are thermally excited and dominate the spectrum. In this chapter, we will focus on the fluctuation spectrum near a weakly damped resonant mode, in order to determine the temperature of the plasma. These modes are Trivelpiece-Gould (TG) standing modes in finite length plasmas.

3.1 Trivelpiece-Gould Modes

In this section, we will review the TG mode conceptually, and show how we characterize the $k_z = 1, 2, 3, \ldots$, $m_\theta = 0$ standing modes by *transmission* experiments. The active excitation allows the modes to be unambiguously identified, making the passive spectral measurements conceptually simpler.

3.1.1 Theory Review

Before we talk about Trivelpiece-Gould (TG) modes, we first consider plasma oscillations in an electron plasma with no boundary. Imagine a displacement of charge fluctuations $+\delta n$ and $-\delta n$, separated by the distance k^{-1} as illustrated in

Figure 3.1(a) top. This k is a wave number. $+\delta n$ denotes an excess of electrons. All electric field lines that comes out of the $-\delta n$ are connected to $+\delta n$, and therefore all the electric field contributes to force on the $+\delta n$. In such a case, there is no oscillation below the plasma frequency ω_p, as shown in Figure 3.1(a) bottom.

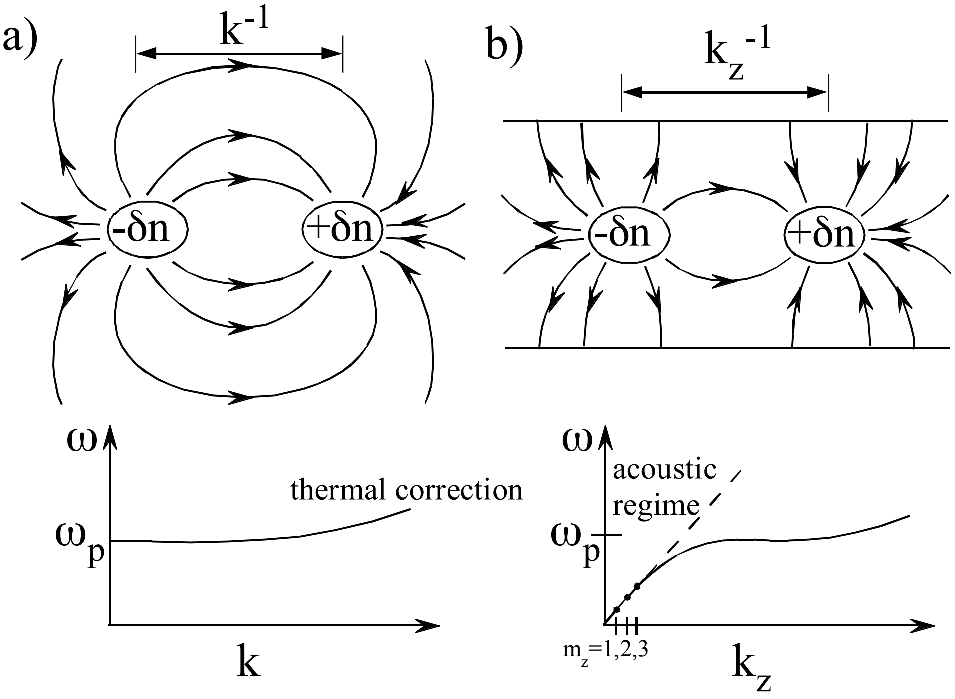

Figure 3.1: Cartoon of the electric field and resulting plasma wave dissipation when $+\delta n$ and $-\delta n$ is displaced by k^{-1} in (a) a plasma without boundary, and (b) a plasma which is confined by a conducting cylinder wall.

Now we consider the case that the plasma is confined in a conducting wall cylinder. Some of the electric field lines are terminated on the cylinder as shown in Figure 3.1(b) top. This reduces the restoring force on the δn, and lowers the wave frequency. The electrostatic wave propagating in a conducting wall is called a TG mode [43]. The dispersion relation of the wave in z direction is shown in Figure 3.1(b) bottom. More electric field is terminated at the cylinder when $-\delta n$ and $+\delta n$ are separated farther (smaller k_z), and the oscillation frequency reaches to zero when k_z reaches to zero.

In this thesis, we identify the TG mode by 3 mode numbers: m_z, m_θ, m_r. A cartoon of the lowest 3 modes are shown in Figure 3.2. For m_z and m_r, the number of nodes gives the mode number. For m_θ, number of peaks in δn versus θ gives the mode number m_θ. In this thesis, we will focus on $m_\theta = 0$, $m_r = 1$ and $m_z = 1, 2, 3$ because these have the strongest coupling to our cylindrical wall antennae (Figure 2.1.

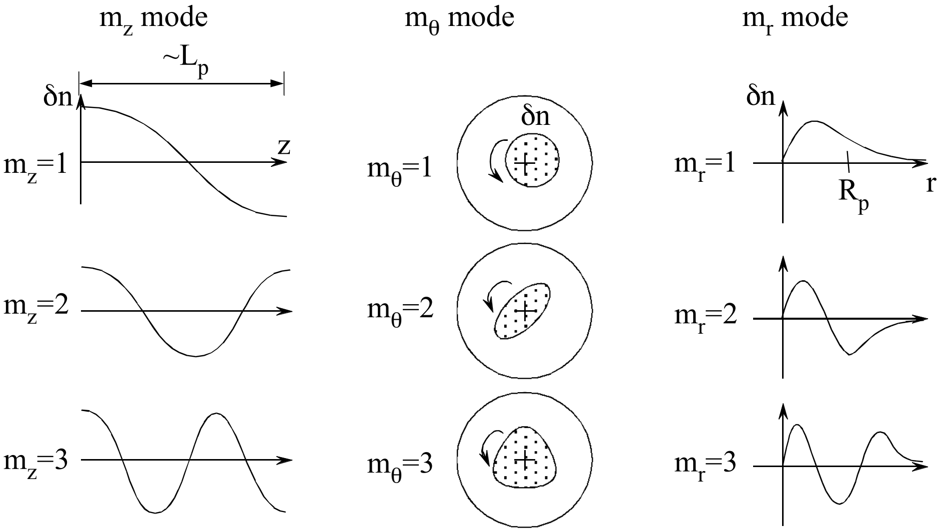

Figure 3.2: Cartoon of δn in the directions of z, θ and r.

In the limit of $k_z\lambda_D \ll 1$ and $R_p k_z \ll 1$, the frequencies of the Trivelpiece-Gould mode resonances for $m_\theta = 0$ and $m_r = 1$ can be approximated as:

$$\omega_m \approx \omega_p \left(\frac{R_p}{R_w}\right)(R_w k_z)\left[\frac{1}{2}\ln\frac{R_w}{R_p}\right]^{1/2}\left[1 + \frac{3}{2}\left(\frac{\bar{v}}{v_\phi}\right)^2\right], \tag{3.1}$$

with damping

$$\gamma \approx -\sqrt{\frac{\pi}{8}}\,\omega\left(\frac{v_\phi}{\bar{v}}\right)^3 \exp\left\{-\frac{1}{2}\left(\frac{v_\phi}{\bar{v}}\right)^2\right\} \tag{3.2}$$

The wave frequencies scale with the plasma frequency $f_p \equiv \omega_p/2\pi = 28$ MHz $(n/10^7\ \mathrm{cm}^{-3})^{1/2}$, reduced by the fill ratio R_p/R_w and by the trap radius compared to the axial wavelength. [7] The modes that travel along z are typically described theoretically in the "infinite length" limit, where they would be written as $\delta n \sim A\delta n(r)\exp(ik_z z - i\omega_m t - \gamma_m t)$. The axial wave numbers for resonant standing modes in length L_p are given approximately by $k_z = \pi m_z / L_p$, where axial mode number is $m_z = 1, 2...5$. We have also included thermal corrections, which depend on the ratio of $\bar{v} \equiv (T/m)^{1/2}$ to the wave phase velocity v_ϕ, where $v_\phi \approx \omega_m / k_z$ is ill-defined to the extent that k_z is approximate.

3.1.2 Transmission Mode Spectra

A schematic of the transmission measurement is shown in Figure 3.3. We perform transmission experiments by applying a sinusoidal voltage at frequency f with amplitude $V_{\rm exc}$ to a cylindrical electrode at one end of the electron plasma column. $V_{\rm exc}$ excites density perturbations δn in the column, which propagate axially and induce the measured voltages V_a on a distant cylindrical antenna with finite load impedance. Here, the wave excitation cylinder has length $L_{\rm exc} = 5.8$ cm,

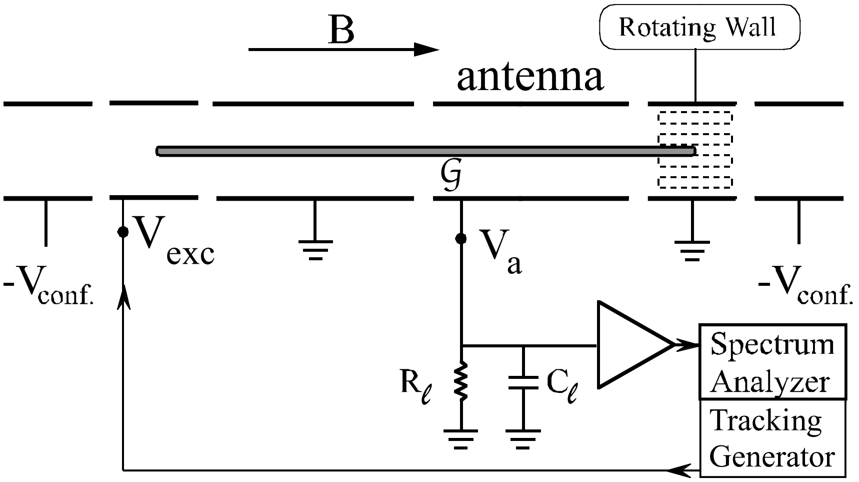

Figure 3.3: Schematic of the transmission measurement.

and the cylinder used as a antenna has $L_a = 11.7$ cm. The load impedance on IV (or EV) is $R_\ell = 690\ \Omega$ in parallel with $C_\ell = 440$ pF (or 190 pF). Plasma parameters were $B = 3$T, L_p=41cm, $n_0 = 10^7\text{cm}^{-3}$ and $T_p = 0.15$eV.

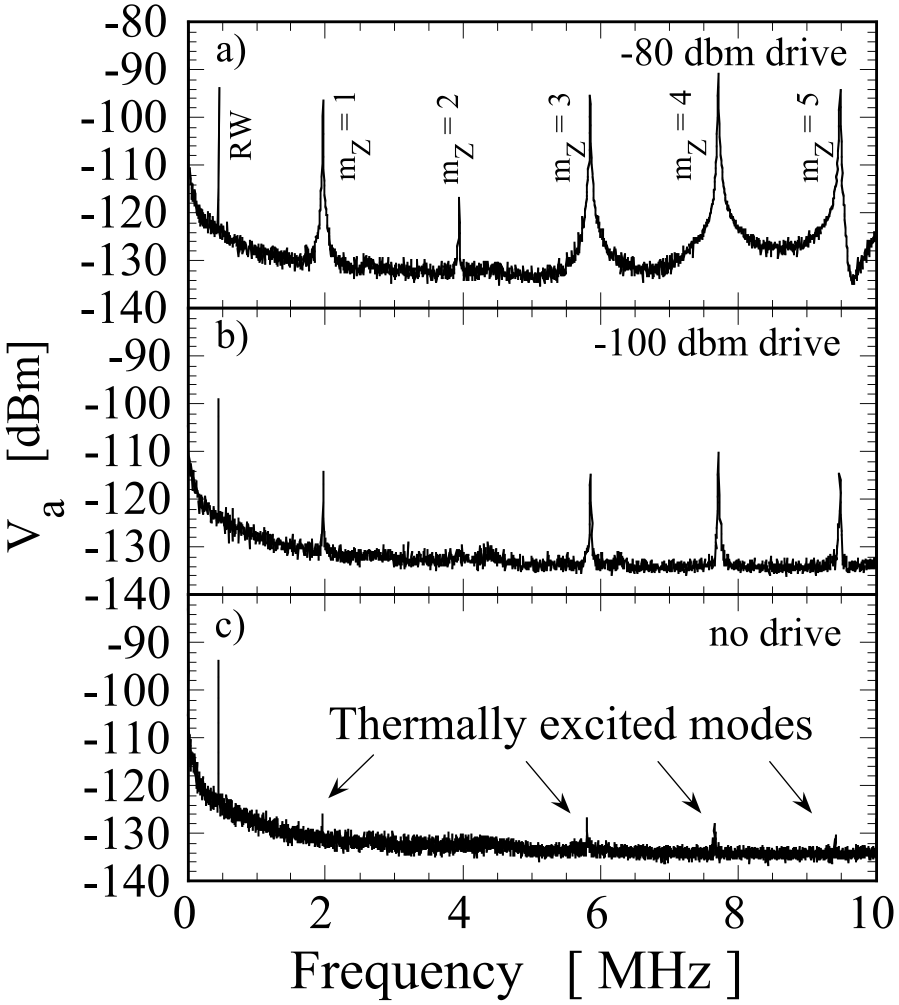

Figure 3.4: Spectrum of $m_r = 1, m_\theta = 0$, $m_z = 1$, 2, ..., 5 Trivelpiece-Gould modes for 3 drive amplitudes including no drive, i.e. thermally excited.

Figures 3.4(a) and 3.4(b) show the spectrum of azimuthally symmetric $m_\theta = 0$ standing Trivelpiece-Gould modes excited by wall excitations of $V_{\text{exc}} = -80$ dbm (22 μV) and -100 dBm (2.2 μV) at frequencies $f = 0.01 - 10$ MHz.

The antenna/mode coupling is essentially the capacitive coupling $\mathcal{G}$ between the cylindrical wall antenna and the radially centered plasma, weighted by $\sin(k_z \cdot z)$ mode dependence. This $\mathcal{G}$ is defined in Eq. (3.4) and the aspect of capacitive coupling is illustrated in Appendix C. The lesser sensitivity for $m_z = 2$ apparent in Figure 3.4 is because this particular detection antenna of length L_a is centered around a node.

The peak amplitudes received for the continuously driven sinusoidal modes are independent of the bandwidth (BW = 3 kHz) of the spectrum analyzer; whereas the spectral amplitude of the inter-mode noise decreases as $(\mathrm{BW})^{-1/2}$, as will be explained in §**??**. At $V_{\mathrm{exc}} = -100$ dBm, the mode fluctuations have amplitude $\delta n/n \sim 10^{-5}$. The peak labeled RW at 450kHz is an artifact of the non-resonant rotating wall drive with $m_\theta^{drive} = 2$. The $m_\theta = 0$ mode measurements presented here have also been obtained with the drive off, and there appears to be no significant coupling between the weak RW drive and the weak T-G modes at incommensurate frequencies.

These modes exhibit exponential damping at a rate γ_{tot} which will be seen in Eq. (3.3) to be the sum of γ_m from inherent plasma mode effects such as Landau damping, and γ_ℓ due to dissipative loading by the amplifier.

3.2 Emission Spectra

Small peaks representing thermally excited modes are still visible in Figure 3.4(c) when the transmitter electrode is grounded ($V_{\mathrm{exc}} = 0$). These peaks have spectral amplitudes on the antenna of $V_a = -124$ dBm measured over a bandwidth of 3 kHz, representing voltage fluctuations on the electrode with spectral density $V_a/\sqrt{df} \approx 2.6nV/\sqrt{\mathrm{Hz}}$. Here, the apparent mode amplitudes scale as $BW^{-1/2}$ as expected for $BW < \gamma$, since the apparent power ($\propto V_a^2$) is a fraction BW/γ of the total mode power in the antenna circuit. (see Appendix A for more detail) These peaks are the thermally excited modes. We now focus on the $m_z = 1$ mode in

Figure 3.4.

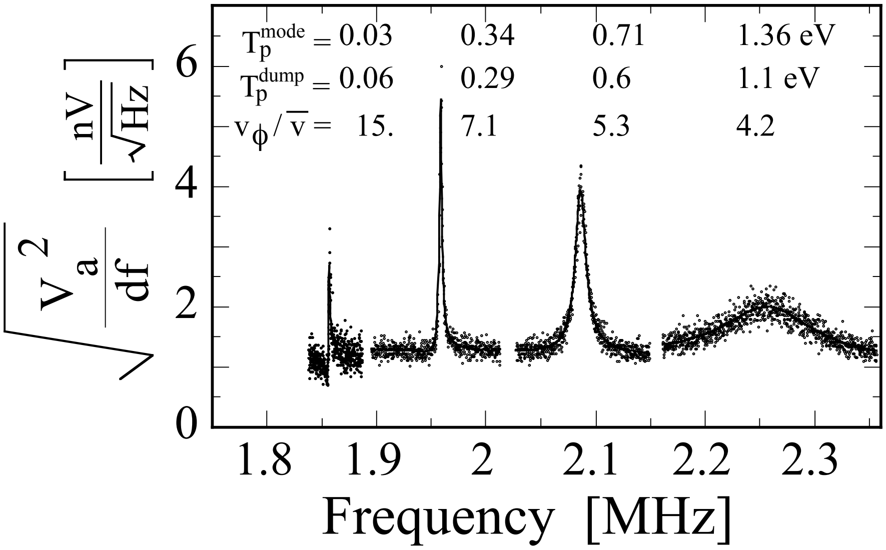

Figure 3.5: Spectra of the thermally excited $m_r = 1, m_\theta = 0$, $m_z = 1$, mode for different plasma temperatures; the solid lines are fits to Eq. (3.16). The temperature T_p^{mode} is from emission measurement. The temperature T_p^{dump} is from standard dump technique.

Figure 3.5 shows received spectra of the thermally excited $m_z = 1$ mode for 4 different plasma temperatures from 0.03 to 1.4eV. The spectra are nominally Lorentzian for these weakly damped modes. The mode frequency f_m increases by 20% with the elevated temperature, as expected from Eq. (3.1). The half width at relative amplitude $(1/\sqrt{2})$ of the spectral peak represents the total damping, γ_{tot}. This total damping consists of the internal *"mode"* damping γ_m and the external *"load"* damping γ_ℓ:

$$\gamma_{\text{tot}} \equiv \gamma_m + \gamma_\ell. \tag{3.3}$$

Here the internal damping is predominantly Landau damping, but any other internal damping (e.g. collisional) would also be included in γ_m. The width of the peaks in Figure 3.5 increases substantially as Landau damping becomes significant for $T_p \geq 0.5$ eV, i.e. for $v_\phi/\overline{v} \lesssim 5$. Additionally, a substantial distortion of the Lorentzian plasma mode is observed for the lowest temperature shown in Figure 3.5; this will be seen to represent load noise reflected by the plasma. This reflected noise adds out of phase on the low frequency side and adds in phase on the higher frequency side, resulting in a spectral shape of a "dip and a peak".

Figure 3.10(b) shows a circuit modeling the reception of thermal noise from the plasma. Near a resonant mode at frequency ω_m with intrinsic damping γ_m, the ratio of antenna current to voltage (i.e., the plasma/antenna admittance) Z_p^{-1}, is well approximated by a simple pole Z_m^{-1}, as

$$Z_p^{-1}(\omega) \sim Z_m^{-1}(\omega) = \frac{\mathcal{G}\omega_m^2}{i(\omega - \omega_m) + \gamma_m}. \tag{3.4}$$

Z_p^{-1} is the admittance of the plasma at all frequencies and Z_m^{-1} is an approximation that is true only near mode frequency ω_m. $\mathcal{G}$ is the geometric (capacitive) coupling coefficient between the plasma mode and the receiving electrode; here $\mathcal{G} \approx 0.5$ pF (or 0.45 cm in CGS units). This is discussed further in Appendix C. On resonance, the mode impedance is real with magnitude

$$R_m \equiv Z_m^{\mathrm{Re}}(\omega_m) = \gamma_m/\mathcal{G}\omega_m^2, \tag{3.5}$$

where we use the following notation $Z^{\mathrm{Re}} \equiv \mathrm{Re}\{Z\}$ and $Z^{\mathrm{Im}} \equiv \mathrm{Im}\{Z\}$. Near ω_m, this may be written $Z_m(\omega) \sim R_m + i(\omega - \omega_m)/\gamma_m$

The external electronics (load) has a measured input resistance R_ℓ and capacitance C_ℓ, or a total load impedance Z_ℓ given by

$$Z_\ell^{-1}(\omega) = R_\ell^{-1} + i\omega C_\ell. \tag{3.6}$$

This is essentially constant over the mode resonance, since $f_{R_\ell C_\ell} \equiv (2\pi R_\ell C_\ell)^{-1}$=0.5MHz for IV (1.4MHz for EV) satisfies $f_{R_\ell C_\ell} < f_m$. That is, the load is essentially capacitive and non-resonant. This load impedance is easily measured with a vector impedance meter. This almost constant Z_ℓ differs from the resonant-circuit loads commonly used in harmonic traps with a small number of particles, [44] simplifying the spectral interpretation somewhat.

3.3 Review of Nyquist theorem

We use Nyquist approach to calculate the fluctuation spectrum. We will review the Nyquist theorem and consider the spectral shape for the impedance with simple pole Z_m in Eq. (3.4) in this section. Figure 3.6 summarizes the Nyquist theorem for simple resistor and for Z_m.

A resistor in thermal equilibrium at temperature T generates fluctuating voltage (current) across the resistor due to the random motion of the electrons. The Thevnin (Norton) equivalent circuit sees this resistor as a voltage (current) source in series (parallel) with a resistor shown in Figure 3.6(a)((b)) [16, 30, 36]

The Nyquist theorem for the Thevnin equivalent circuit states that the mean square voltage $< V^2 >$ across a resistor R, in thermal equilibrium at temperature T is given by

$$\begin{aligned} < V^2 > &= 4\,\mathrm{k_B}\,\hat{T}\,R\,BW \\ &= 4\,T\,R\,BW \end{aligned} \tag{3.7}$$

where $\hat{T}$ is the temperature in $[^\circ K]$ while we express temperature T in energy unit [J]. we note that temperature of the plasma T_p is normally expressed in [eV] in this thesis, therefore one needs to multiply with 1.6×10^{-19} calculating the fluctuation of plasma. BW is the frequency bandwidth within which the mean voltage fluctuations $< V^2 >$ are measured.

For the Norton equivalent circuit, the mean squared current $< I^2 >$ across a resistor R is proportional to the admittance R^{-1}, as

$$< I^2 >= 4\,T\,R^{-1}\,BW \tag{3.8}$$

The original Nyquist theorem is easily generalized for any linear passive element whose complex impedance is $Z(f)$. The power spectral densities are now

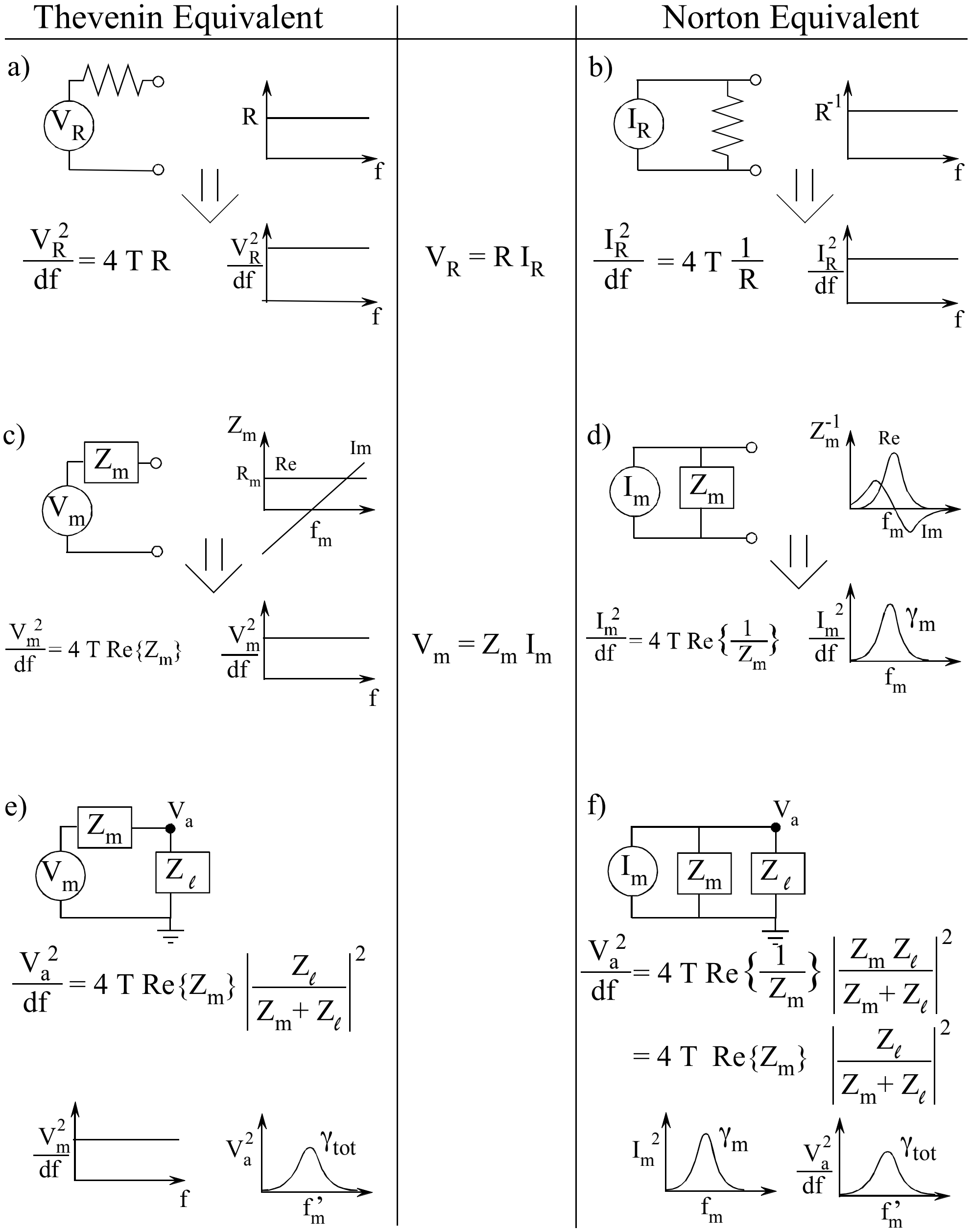

Figure 3.6: Thevenin and Norton equivalent circuit model of Johnson noise with Z_m having the form of Eq. (3.4) voltage V and current I are the average value.

expressed as

$$\begin{aligned} \frac{V^2}{df} &= 4T\ \mathrm{Re}\{Z\}, \quad \textit{and} \\ \frac{I^2}{df} &= 4T\ \mathrm{Re}\{Z^{-1}\} \end{aligned} \tag{3.9}$$

Figure 3.6 (c) and (d) shows a case with a simple pole for Z_m as in Eq. (3.4). $\frac{V_m^2}{df}$ is still constant versus frequency, but $\frac{I_m^2}{df}$ is now a Lorentzian with center frequency ω_m and width γ_m.

In order to measure the voltage, we must connect a load Z_a to Z_m as shown in Figure 3.6(e) and (f). The signal at the amplifier V_a is the voltage V_m reduced by the voltage divider ratio $\frac{Z_\ell}{Z_m+Z_\ell}$. Therefore,

$$\frac{V_a^2}{df} = 4\,T\,Z_m^{\mathrm{Re}} \left|\frac{Z_\ell}{Z_m+Z_\ell}\right|^2. \tag{3.10}$$

Using Eq. (3.4),

$$\frac{V_a^2}{df} = 4\,T\,Z_m^{\mathrm{Re}} \left|\frac{Z_\ell}{Z_m^{\mathrm{Re}}+Z_\ell^{\mathrm{Re}}}\right|^2 \frac{\gamma_{tot}^2}{\gamma_{tot}^2+(\omega-\omega_m')^2}, \tag{3.11}$$

here,

$$\begin{aligned} \gamma_{\mathrm{tot}} &\equiv \gamma_m+\gamma_\ell = \left(1+\frac{Z_\ell^{\mathrm{Re}}}{R_m}\right)\gamma_m, \\ \delta\omega_m &\equiv \omega_m-\omega_m' \equiv Z_\ell^{\mathrm{Im}}\ \omega_m^2\ \mathcal{G}. \end{aligned}$$

Figure 3.6(f) illustrates that the imaginary part of the load, Z_ℓ^{Im}, shifts the mode frequency f_m to f_m'; and the real part of the load, Z_ℓ^{Re}, increases the damping γ_m to γ_{tot}. Both Thevenin and Norton equivalent circuits give the same measured power spectral density $\frac{V_a^2}{df} = 4\,T\,Z_m^{\mathrm{Re}} \left|\frac{Z_\ell}{Z_m+Z_\ell}\right|^2$.

3.4 Determination of Z_p

In order to determine the temperature from the measured power spectral density $\frac{V^2}{df}$ using the Nyquist theorem, we need to determine Z_p. In this section, we will discuss how to measure the $Z_p(\omega)$ directly with reflection/absorption measurement; and then, show how to model Z_p near a mode with simple pole $Z_m(\omega)$.

3.4.1 Reflection/Absorption measurement

A direct measurement of Z_p is obtained with a reflection/absorption measurement, [20] whose schematic is shown in Figure 3.7(a). The direct measurement of Z_p uses a directional coupler and lock-in detector to determine the complex reflection coefficient $r(f)$ for a weak signal at frequency f incident on the receiving antenna and plasma. This reflection coefficient is defined as the voltage fraction (and phase) which is reflected by the plasma-loaded antenna compared to that reflected by an open circuit without antenna or plasma, i.e.

$$r \equiv \frac{V_{\rm refl}(\text{plasma})}{V_{\rm refl}(\text{open})}. \tag{3.12}$$

This reflection coefficient depends on the impedance $Z_{\rm pc}$ connected to the directional coupler compared to the impedance $Z_0 = 50\ \Omega$ of the coupler itself, and is given implicitly by

$$Z_{\rm pc} = Z_0 \frac{(1+r)}{(1-r)}\ . \tag{3.13}$$

Here, $Z_{\rm pc}^{-1} = Z_p^{-1} + i\omega C_\ell$ is the total admittance of the plasma-loaded antenna, given by the plasma admittance Z_p^{-1} of Eq.(3.4) in parallel with the capacitive admittance $i\omega C_\ell$ of the electrode and connecting cable.

Figure 3.7(b) shows the measured amplitude and phase of the reflected signal for an EV plasma as the frequency is scanned across the $m_z = 1$ mode. The entire signal is reflected at frequencies f far from the mode frequency f_m, because the plasma impedance [Eq. (3.4)] is large off-resonance, i.e. $|Z_p(f)| \gg Z_0$. On resonance, 37% is reflected and about 63% of the incident wave is absorbed by the plasma. In essence, the depth of the reflection dip indicates how close R_m is to the 50 Ω of the directional coupler, since $Z_m^{\rm Im}(f_m) = 0$. A fit (solid line) to the $r(f)$ data using the simple pole Z_m in Eqs. (3.4) and (3.13) gives the parameters of $Z_{\rm pc}$ as $R_m = 111\ \Omega$, $f_m = 4.073$ MHz, $\gamma_m/\omega_m = 1.15 \times 10^{-3}$, and $C_\ell =$ 145 pF, resulting in $\mathcal{G} = \gamma_m/(\omega_m^2 R_m) = 0.41$ pF (or 0.37 cm in CGS).

Figure 3.7(c) shows the reflection measurement with a launched rf wave that has larger amplitude (-90dBm) than (b). The damping is smaller by a factor

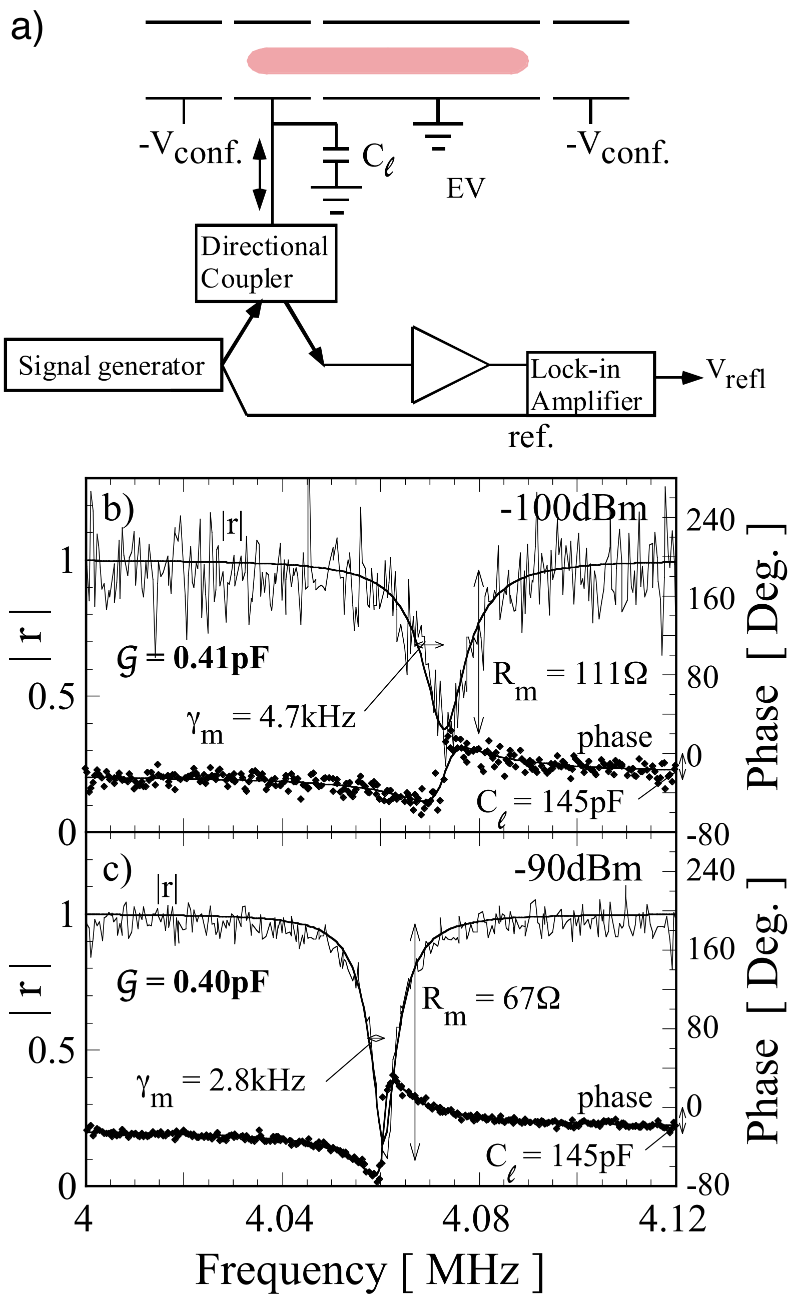

Figure 3.7: (a) Schematic of reflection/absorption measurement with a launched sinusoidal wave. (b)Measured reflection coefficient $|r|$ and it's phase with fits to Eq. (3.4), with rf at -100dBm. (c)Same rf at -90dBm. The parameters G, C_ℓ, f_m are robust; whereas R_m and γ_m vary, since Landau damping decreases with wave amplitude. Plasma parameters were T_p =1.4eV, n_0=1.2×10$^7 cm^{-3}$, L_p =23cm, R_p=1.4cm.

of 2 because the launched wave is so large that particles are trapped in the wave, and therefore Landau damping is suppressed.[Danielson] This large amplitude wave leads to a smaller measured value of Z_p (e.g. $R_m = 60\Omega$ instead of 111Ω). However, the measured coupling coefficient $\mathcal{G}$ is the same, because $\mathcal{G}$ is purely geometrical and doesn't depend on the damping.

Figure 3.8 shows that the measured plasma impedance R_m increases to much larger than 50Ω as the temperature increases, as expected from strong Landau damping at high temperatures. The geometric capacitive coupling coefficient is independent of temperature also as expected. In practice, large amplitude rf gives better S/N in measurement of robust parameter $\mathcal{G}$ because when Landau damping is suppressed by trapping effect, the impedance is close to 50Ω at f_m. However, this large amplitude obscures the fragile parameters R_m and γ_m as already mentioned.

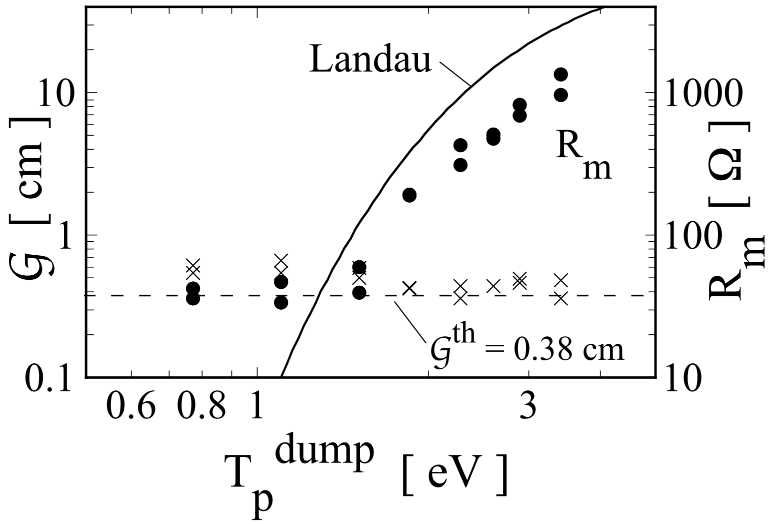

Figure 3.8: Coupling coefficient $\mathcal{G}$ and plasma-mode impedance R_m versus plasma temperature.

Figure 3.8 shows that the coupling coefficient $\mathcal{G}$ is robust, i.e. it changes by less than a factor of 2 when the plasma temperature changes from 0.7 eV to 3.5 eV. The simple low temperature limit of Eq. (3.17), for EV plasma parameters, gives

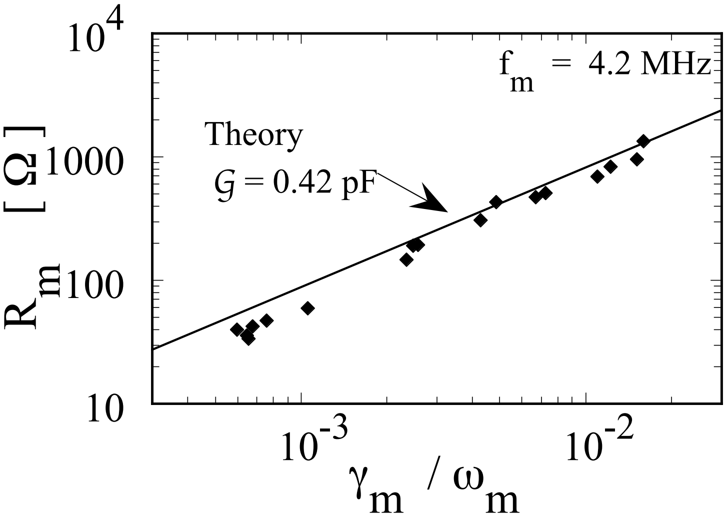

Figure 3.9: Normalized plasma mode impedance versus the plasma-mode damping rate.

$\mathcal{G} = 0.42$ pF, shown with a dashed line. In contrast, the mode impedance R_m varies from 30Ω to 2000Ω in that temperature range, as Landau damping increases the mode damping γ_m. Since $\mathcal{G}$ is almost constant, Eq. (3.5) predicts that R_m will increase as γ_m/ω_m^2. The solid line represents $R_m = \gamma_{\text{Landau}}/\omega_m^2\mathcal{G}$, where γ_{Landau} is calculated from plasma parameters (see Appendix C). The discrepancies may be due to a 20% error in the temperature calibration of the EV apparatus, or possibly finite length plasmas may require a correction to Landau damping as described in more detail in §4.7.

Figure 3.9 illustrates that the measured R_m (from the depth of the refrection dip) is directly proportional to the measured mode damping γ_m (from the width of the reflection dip); here again the dashed line is the simple theory prediction $\mathcal{G} = 0.42$ pF.

3.5 Temperature Determination from Mode Spectrum

Now we are ready to determine the temperature of the plasma from the fluctuation spectrum. Figure 3.10(a) shows the schematic diagram of plasma emission measurement. We use an interior cylinder as the "passive" receiver antenna. This antenna is connected to the amplifier outside the vacuum chamber with a coax cable. This coax cable is approximated as an additional capacitance added to the inherent input (load) capacitance of the amplifier, giving a total capacitance C_ℓ. Then the plasma fluctuation signal is amplified with amplifier, then feed to

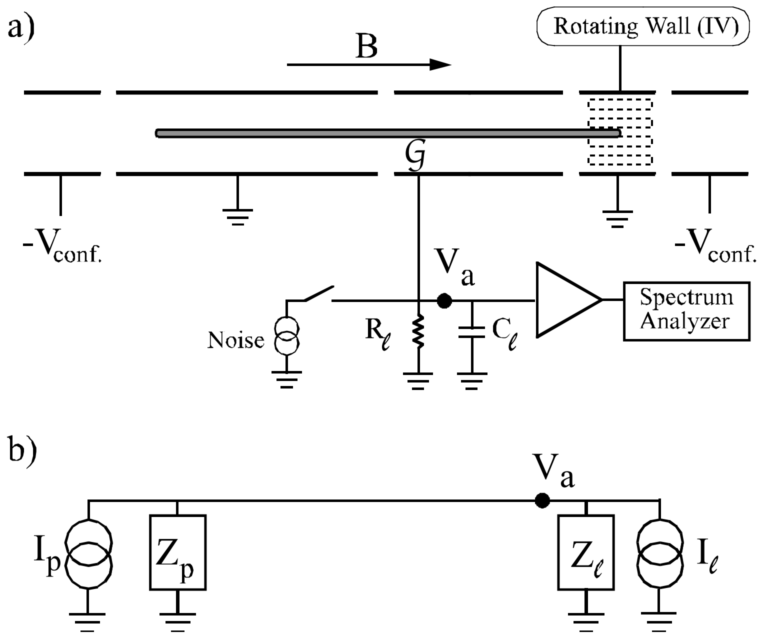

Figure 3.10: (a) Schematic diagram of plasma emission measurement. (b) Electrical circuit analogue to the plasma mode and antenna.

spectrum analyzer.

Figure 3.10(b) shows the Thevenin equivalent circuit for this measurement. This merely adds a noise current source I_ℓ which represents the Johnson noise from the load to a Figure 3.6(f). While both Norton and Thevenin equivalent circuit picture gives the same answer, we used Norton equivalent circuit to describe plasma noise because the plasma density fluctuation induces the image charge on the antenna, which is a current source, rather than a voltage source.

The plasma noise source I_p and the load noise source I_ℓ are added in quadrature because they are not correlated and therefore crossterm vanishes as you take time average. This total noise current then induces V_a as it flow through Z_{tot} which is defined as

$$Z_{tot}^{-1} \equiv Z_m^{-1} + Z_\ell^{-1}. \tag{3.14}$$

Therefore the voltage power spectral density $\frac{V_a^2}{df}$ measured at the antenna is given by

$$\begin{aligned} \frac{V_a^2(f)}{df} &= \left[\frac{I_p^2}{df} + \frac{I_\ell^2}{df}\right] |Z_{tot}|^2 \\ &= \left[4T_p \mathrm{Re}\{Z_p^{-1}\} + 4T_\ell \mathrm{Re}\{Z_\ell^{-1}\}\right] \left|\frac{Z_p\, Z_\ell}{Z_p + Z_\ell}\right|^2 . \end{aligned} \tag{3.15}$$

Using Eqs. (3.3), (3.4), (3.6), and (3.14), Eq. (3.15) can be explicitly written as

$$\begin{aligned} \frac{V_a^2(f)}{df} &= 4T_p R_m \, \frac{|Z_\ell|^2}{|R_m + Z_\ell^{\mathrm{Re}}|^2} \, \frac{\gamma_{\mathrm{tot}}^2}{\gamma_{\mathrm{tot}}^2 + (\omega - \omega_m')^2} \\ &+ 4T_\ell Z_\ell^{\mathrm{Re}} \left\{ 1 - \frac{2(\omega - \omega_m')\delta\omega_m + (\gamma_{\mathrm{tot}}^2 - \gamma_m^2 - \delta\omega_m^2)}{\gamma_{\mathrm{tot}}^2 + (\omega - \omega_m')^2} \right\} \end{aligned} \tag{3.16}$$

The first term of Eq. (3.16) describes the Lorentzian "plasma" emission spectrum centered at ω_m' of width γ_{tot} previously descrived in Eq. (3.11), with amplitude "proportional to" $T_p R_m$. Thus, the emission spectrum alone does not determine T_p unless prior knowledge of the coupling coefficient $\mathcal{G}$ allows R_m to be obtained from Eq. (3.5). For $R_m \gg Z_\ell^{\mathrm{Re}}$, the peak amplitude $\frac{V_a^2}{df}(f_m)$ scales as R_m^{-1}, and the width is $\gamma_m \propto R_m$. For $R_m \ll Z_\ell^{\mathrm{Re}}$, the peak amplitude $\frac{V_a^2}{df}(f_m)$ scales as R_m, and the width is $\gamma_m + \gamma_\ell = (R_m + Z_\ell^{\mathrm{Re}})\mathcal{G}\omega_m^2$.

The second term describes the "load" noise as a uniform background, plus a "dip and peak" from the $\frac{2(\omega-\omega_m')}{\gamma_{tot}^2+(\omega-\omega_m')^2}$ term, plus a Lorentzian absorption, with all 3 spectral components proportional to $T_\ell Z_\ell^{\mathrm{Re}}$. Some of the load noise is "shorted out", or absorbed, by the plasma; some is reflected by the plasma, with a phase shift varying as $\omega - \omega_m$.

Surprizingly, making the load about as "noisy" as the plasma produces the "optimal spectra", allowing a calibrated determination of T_p in one measurement. That is, determination of the antenna/plasma coupling $\mathcal{G}$ requires a reflection/absorption measurement. This can either be a separate measurement using a launched sine wave; or it can be obtained from the "emission" spectrum alone using the naturally launched load noise. This is illustrated in Figure 3.11

Figure 3.11(a) shows the received spectrum of the $m_\theta = 0$, $m_z = 1$ mode in the EV apparatus, when the load is much colder than the plasma. The spectrum is completely described as the sum of the two term in Eq. (3.16), with a Lorentzian "plasma" term and a smaller load noise term (dashed). Since Z_ℓ is known, the spectrum is parametrized by 5 parameters: plasma temperature T_p, mode frequency ω_m, mode damping γ_m, coupling coefficient $\mathcal{G}$ and load temperature T_ℓ. However, the "load" component here is too small for the characteristic dip and peak to give an accurate calibration of the coupling coefficient $\mathcal{G}$. Using $\mathcal{G} = 0.43$ pF (0.39 cm in CGS) from a separate measurement described below, a 4 parameter fit of the data to Eq. (3.16) gives $T_p = 1.89$ eV, $f_m = 4.063$ MHz, $\gamma_m/\omega_m = 2.1 \times 10^{-3}$ and $T_\ell = 0.35$ eV.

Here, we used a Fortran program to calculate the spectrum and fit to the measured spectra. The fitting routine "sNLS1" in the SLATEC library was used to perform on the 4 parameter fit. The purpose of "sNLS1" is to minimize the sum of the squares of M(number of data points) nonlinear functions in N variables by a modification of the Levenberg-Marquadt algorithm. In practice, it convergis

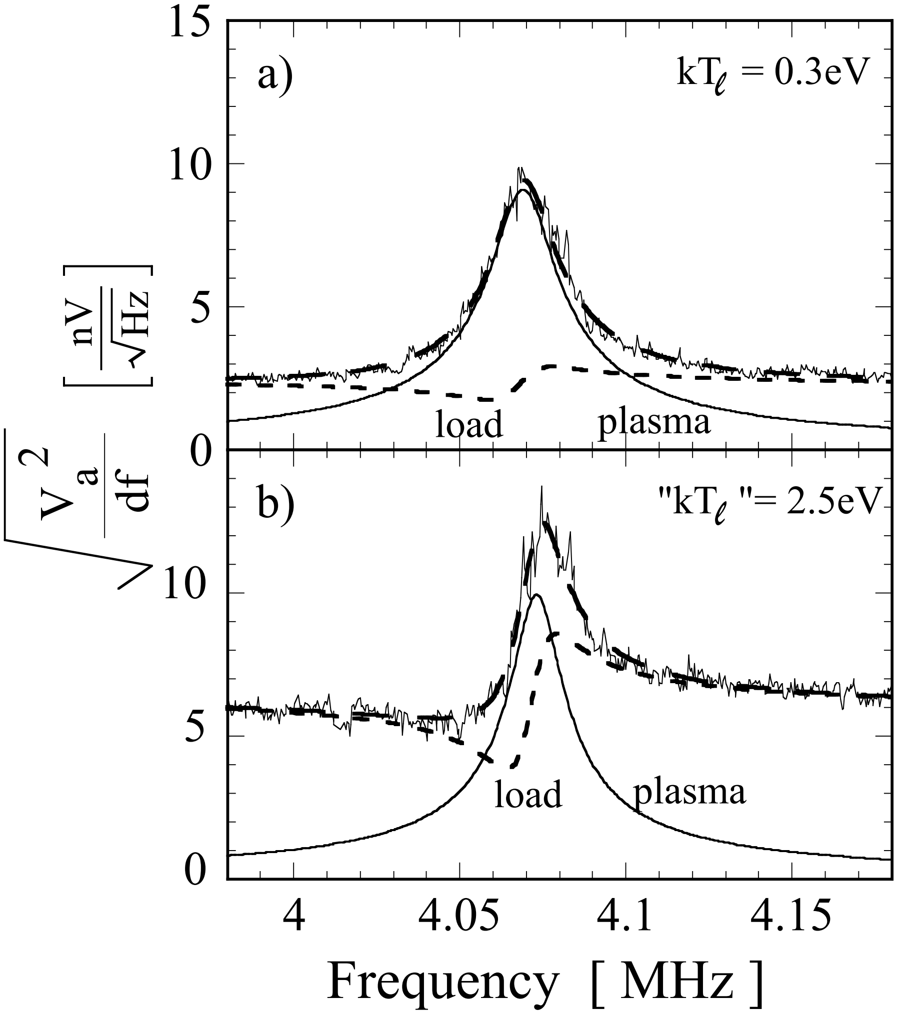

Figure 3.11: (a) Spectra of the thermally excited $m_\theta = 0$, $m_z = 1$ mode for $T_p =$ 1.9 eV and $T_\ell = 0.3$ eV. (b) Same with noise added to the antenna ("T_ℓ" $= 2.5$ eV). The long-dashed line is the full Eq. (3.16) fitted to the data, with the solid line being the plasma component, and the short-dashed line being the load noise filtered by the plasma.

well even if the initial estimates for the parameters are not very accurate.

In Figure 3.11b, noise has been deliberately added to the antenna, corresponding to an effectively higher load temperature. The received spectrum has the same Lorentzian "plasma" component, but the dip and peak from the plasma "shorting" the load noise is more pronounced. This phase-sensitive reflection and absorption of the load noise by the plasma determines the antenna coupling coefficient $\mathcal{G}$. A full 5-parameter fit of the received spectrum of Figure 3.11(b) to Eq. (3.16) then gives $T_p = 1.84$ eV, $f_m = 4.067$ MHz, $\gamma_m/\omega_m = 1.6 \times 10^{-3}$, $\mathcal{G} = 0.43$ pF (0.39 cm in CGS) and $T_\ell = 2.5$ eV. The standard dump diagnostic gives $T_p^{\text{dump}} = 1.9$ eV, with no measureable difference for Figure3.11(a) and (b).

Figure 3.11(b) demonstrates that the plasma temperature can be obtained in one measurement, if the load is "noisy enough." Of course, if the emission from the load were to dominate the spectrum, the plasma component proportional to T_p might be obscured. For Eq. (3.15) to be valid, the load noise must be uncorrelated with the plasma mode. Even a sinewave of constant amplitude which tracks the frequency of the analyzer (from a tracking generator) satisfies the criterion. Thus, the "noise" source in Figure 3.11 can be a sine wave generator. This makes it more apparent that a reflection/absorption measurement is being combined with an emission measurement. In practice, this is often the easiest and most effective source when using a swept analogue analyzer.

We note that the damping rate γ_m is measurably smaller when the noise added to the load drives the mode to large amplitude, because the wave traps particles at the phase velocity, thereby reducing the Landau damping. The thermal components (solid curve on Figure 3.11(b)) can be viewed as small test waves in the presence of a larger amplitude wave excited by the load noise.

We have also calculated the coupling coefficient $\mathcal{G}$ analytically using kinetic theory. Taking a uniform density collisionless plasma of radius R_p with z-periodic boundaries of period L_p, this analysis reproduces the impedance of Eq. (3.4) for frequencies near a plasma resonance. In the limit of $T_p \to 0$, assuming that

$\lambda_D \ll R_p$ and that $k_z R_w \ll 1$, we find that

$$\begin{aligned}\mathcal{G} =& \frac{[4\pi\varepsilon_0] L_p F_m^2}{1 + x^2 \ln^2(R_w/R_p)} \\ \simeq& \frac{[4\pi\varepsilon_0] L_p F_m^2}{1 + 2\ln(R_w/R_p)}\end{aligned} \tag{3.17}$$

Here the sinusoidal mode factor is $F_m \equiv (k_z L_p)^{-1}[\sin(k_z z_2) - \sin(k_z z_1)]$, with z_1 and z_2 representing the left and right ends of the antenna cylinder, measured from the end of the plasma; x is a dimensionless quantity that satisfies the equation $x J_1(x) \ln(R_w/R_p) = J_0(x)$, and is related to the frequency of the plasma mode by $x = k_z R_p(\omega_p^2/\omega_m^2 - 1)^{1/2}$. For $R_w/R_p \gg 1$, one sees $x \approx \sqrt{2/\ln(R_w/R_p)}$, which gives the appsoximate expression in Eq.(3.17).

All equations in this chapter except those for capacitance (e.g. Eq. (3.17)) are equally valid in CGS or SI; in CGS the equations for capacitance would have no $[4\pi\varepsilon_0]$.

Equation (3.17) for $\mathcal{G}$ presumes that the plasma column is penetrating the cylindrical antenna completely. When the antenna is at the end of the plasma and the plasma only partially penetrates the electrode, the plasma end point z_p would replace the electrode end z_2 in estimating F_m.

3.5.1 Digitized FFT spectrum

Alternately, one can use transient digitizer and a numerical FFT to obtain the spectrum, instead of using an analogue spectrum analyzer. We used an 8-bit transient digitizer (Aeon 3248) that digitizes at 10Msample/sec with 32k words memory. Interestingly, more bits of digitization accuracy do not significantly improve the spectral measurement. We put 5MHz low pass filter before digitizer (after the amplifier) to remove the signal above the Nyquist frequency which is 5MHz to avoid aliasing. Figure 3.12(a) shows an example of raw fluctuation data $V_a(t)$. Figure 3.12(b) is the measured probability versus amplitude, with a Gaussian fit. This figure demonstrates that the measured fluctuation is a random signal with Gaussian amplitude distribution.

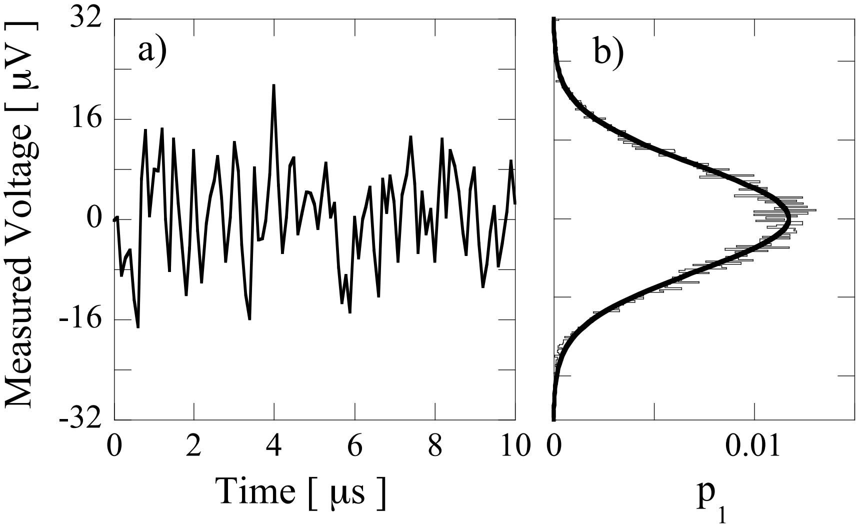

Figure 3.12: (a) Digitized amplitude of the plasma noise. (b) amplitude probability with Gaussian fit.

Figure 3.13(a) shows a cartoon of the signal from N points of data digitized every Δ seconds. For our digitizer, $N = 32,000$ points and $\Delta = 0.1\mu s$, giving a total record time $\tau = 3.2$ms. Discrete Fourier Transformation of $x_k \equiv V_a(k\Delta)$ gives $\widetilde{X}_n$ at N+1 discrete points representing the frequency range $-f_{Nyquist}$ to $f_{Nyquist}$.

$$\widetilde{X}_n \equiv \sum_{k=0}^{N-1} x_k e^{2\pi ikn/N} \tag{3.18}$$

The one-sided magnitude square of $\widetilde{X}_n$, denoted by P_n is

$$\begin{aligned} P_n &= |\widetilde{X}_n|^2 + |\widetilde{X}_{N-n}|^2 \\ &= 2|\widetilde{X}_n^2 \quad [V^2], \end{aligned} \tag{3.19}$$

For $0 < n < \frac{N}{2} - 1$. The discrete version of Parseval's theorem is then

$$\sum_{k=0}^{N-1} x_k^2 = \frac{1}{N} \sum_{n=0}^{N/2-1} P_n \tag{3.20}$$

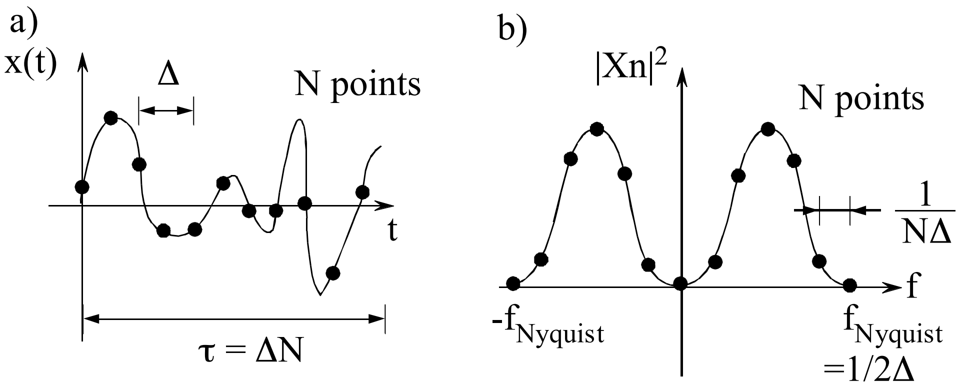

Figure 3.13: (a) Cartoon of the discrete signal. (b) and it's Fourier transformed spectrum.

Finally, the discrete power spectral density $\left(\frac{V^2}{df}\right)_n$ is defined as

$$\begin{aligned}\left(\frac{V^2}{df}\right)_n &\equiv \frac{1}{\tau}P_n\Delta^2 \\ &= 2\frac{\Delta}{N}|\widetilde{X}_n|^2\end{aligned} \tag{3.21}$$

Figure 3.14 shows the "digital" spectrum is obtained from a plasma similar to that used in Figure 3.7, but with a different $T_p = 0.96$ eV. White noise current was added on receiver as in Figure 3.10, with average amplitude corresponding $T_\ell = 1.1$eV.

Figure 3.14(a) was obtained as follows. 0.3 second after the inject of the plasma, 1) the digitizer recorded data for 3.2 ms. 2) The recorded data was transformed to a computer through CAMAC. Steps 1) and 2) were repeated 3 times. This required 132ms to take the 96k words of data. Then we calculate the discrete power spectral density $\frac{V^2}{df}$ using N=96k; giving an effective BW=10MHz/N=104Hz. These spectral conponents are then averaged over 100 conponents (10kHz), resulting in a Signal-to-noise of $S/N = \sqrt{\frac{10\,kHz}{104\,Hz}} \sim 10$.

Figure 3.14(b) is obtained with spectrum analyzer with parameters BW=10kHz, video filter=100Hz, total scan time =0.5 sec. S/N for this spectrum analyzer measurement is given by $S/N = \sqrt{\frac{video\,filter}{BW}} = 0.1$. There are 10 times more data points in (b) than (a) because we digitized 10 points in $\frac{1}{video\ filter}$=0.01 sec. We can see from the Figure 3.14 that these 2 spectra have about the same S/N.

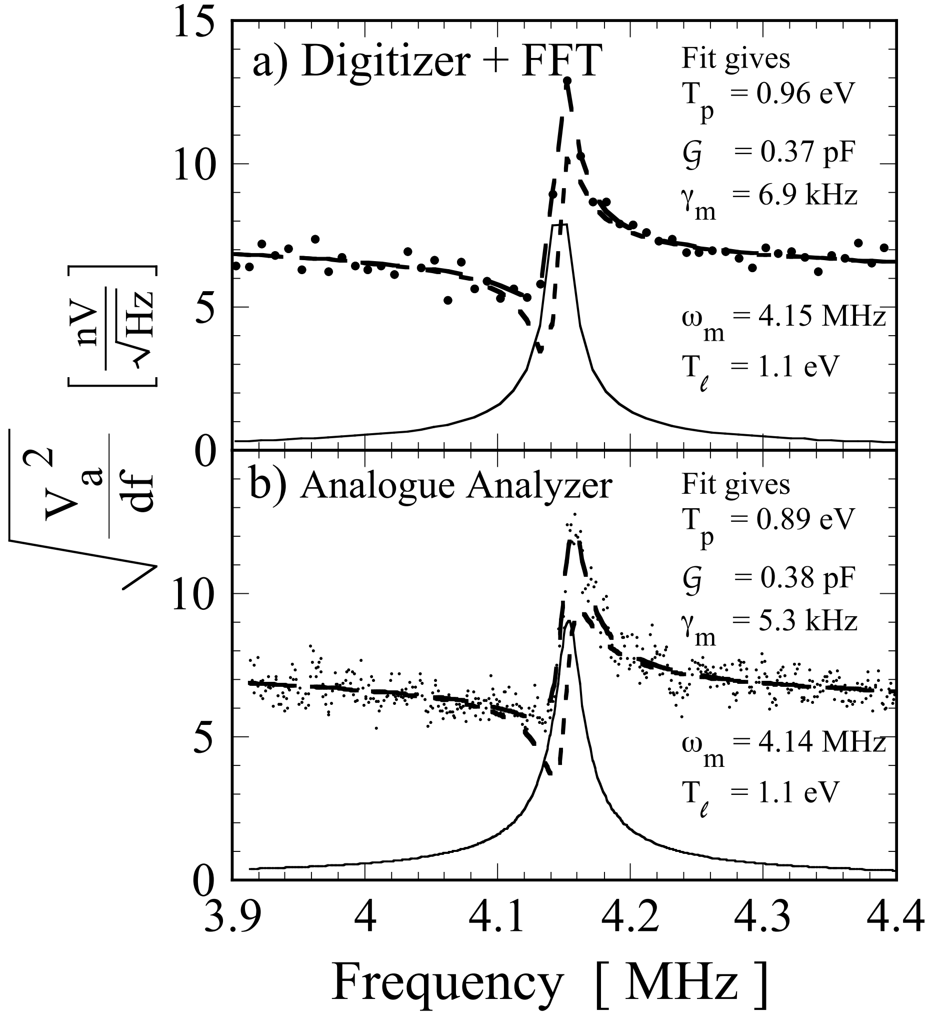

Figure 3.14: (a) Mode spectrum obtained with transient digitizer and a numerical FFT; (b) the same spectrum obtained with an analogue spectrum analyzer.

It takes 50 times loner time to get the same S/N for spectrum analyzer because spectrum analyzer is using only 10kHz BW worth of spectrum out of the scan range of 0.5MHz. This ratio of BW versus scan range, 1/50 is the same factor that the spectrum analyzer is 50 times inefficient compared to the transient digitizer.

Once obtained the power spectral density, we can perform the same fitting to Eq. (3.16). The result of fit is in the figure, showing that both methods gives the same result.

3.6 Mode spectrum Temperature Diagnostic

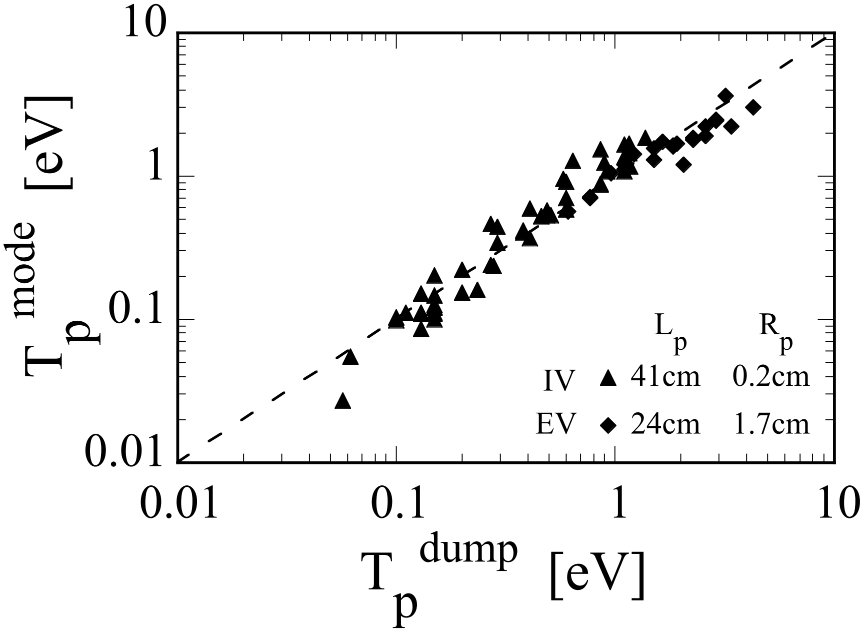

Figure 3.15: Plasma temperature measured by mode emission technique, compared to the standard dump temperature measurement. The triangles are from the IV apparatus and the diamonds are from the EV apparatus.

Figure 3.15 displays the plasma temperature T_p^{mode} obtained from the emission spectra near a mode versus the plasma temperature T_d^{dump} measured by dumping the plasma. Data was taken for plasmas with a range of "geometric" parameters (n, R_p, L_p) on both EV (circles) and IV (triangles), with varied amounts of plasma heating. Most of the values of T_p^{mode} were obtained from a 4-parameter fit to the emission spectra, together with a separate measurement of $\mathcal{G}$ for each (n, R_p, L).

On IV, the value of $\mathcal{G}$ was determined from a single 5-parameter fit to the non-Lorentzian "$T = 0.06$ eV" spectrum of Figure 3.5, giving $\mathcal{G} = 0.21$ pF (0.19 cm in CGS).

Implementation of the "high temperature load" technique has obviated the directional coupler reflection measurements, and essentially identical values of T_p are obtained with a single spectrum.

Figure 3.15 demonstrated that T_p^{mode} and T_p^{dump} agrees well over a wide range of plasma parameters. We conclude that the mode emission spectra determines the temperature of plasma with about ±15% error; here we note that measurement of T_p^{dump} itself typically has ±15% error.

4

Temperature diagnostic in a strongly damped mode regime

In the previous chapter, we focused on the spectrum near a weakly damped mode (with $\frac{\gamma}{\omega_m} < 0.1$) and modeled the mode spectral shapes with Lorentzians. When the mode is strongly damped, the spectrum deviates substantially from a Lorentzian. Here, we present the first experimental studies of the complete spectrum of a trapped plasma near thermal equilibrium.

We measure the thermal emission spectrum over a broad frequency range (0.5-18MHz) encompassing the lowest 5 to 7 plasma modes. A kinetic theory calculation of Z_p [10, 21] incorporating Landau damping describes the spectra very well, both in the strongly damped and weakly damped mode regimes, so long as plasma is long compared to the radius of plasma (i.e. $\frac{L_p}{R_p} \gtrsim 20$). However, the kinetic theory overestimates the actual Landau damping when the plasma is short ($\frac{L_p}{R_p} \lesssim 20$), and therefore underestimates the temperature. For short plasmas ($10 < L_p/R_p < 20$), our experiments show that Landau damping may be 10 times less than "expected"; this may be interpreted as due to a 10-20% ambiguity in k_z.

We also determine the plasma temperature by comparing the total (frequency-integrated) fluctuation measurements to calculations based on thermodynamic theory [12]. The thermodynamic argument is robust, in that it does not depend on the shape of the spectrum; but it requires that we separately determine the plasma parameters n, L_p, and R_p.

4.1 Apparatus with Transmission Cable Model

When we look at high frequencies, we need to calibrate for the transmission line resonance, since the wavelength of the signal in the cable becomes comparable to the cable length. The experiments here were performed in the same apparatus as in the previous chapter, with more rigorous 50Ω termination of cables at the outside of the machine; but conceptually, we need to be more complete.

Figure 4.1 shows the apparatus with a more complete electronic model and its equivalent circuit. The transmission line and capacitance between antenna and neighboring cylindrical electrodes C_n are conceptually added onto Figure 2.1(a). In this chapter, we used EV apparatus only, whose parameters are $B = 0.375$kG, $R_p = 1.0 \rightarrow 1.7$cm, R_w=3.8cm, $n \sim 8 \times 10^6 \text{cm}^{-3}$, $L_p = 15 \rightarrow 37$cm.

For some spectrum measurement, all of the coax cables other than the one connected to the antenna were terminated outside of the vacuum chamber with 50Ω in order to avoid the transmission cable resonance which causes unwanted extra noise on antenna above 10MHz. The difference is shown in Figure 4.7)(shorted cables) and Figure 4.6(b)(50Ω terminated). The resistive damping of the mode caused by these 50Ω termination $\frac{\gamma}{\omega_m} \sim \mathcal{G}\omega_m R_{50\Omega}$(see Eq.(3.5)) is estimated to be about 10^{-3}, which is comparable to the internal plasma damping for weeakly damped plasma modes. This means that for low temperature plasmas where damping is weak, the measured damping can be doubled compared to the internal plasma damping.

Figure 4.1(b) is the circuit analogue of Figure 4.1(a). We now separate the load impedance Z_ℓ in previous chapter Figure 2.1 into 3 parts. 1) Z_n is the impedance to the "next" cylinder, i.e. from the antenna through the neighbor cylinder, then terminated to ground with 50Ω. 2) The transmission cable from the antenna to the receiver amplifier is modeled with a repeating LCR circuit. 3) The impedance Z_ℓ

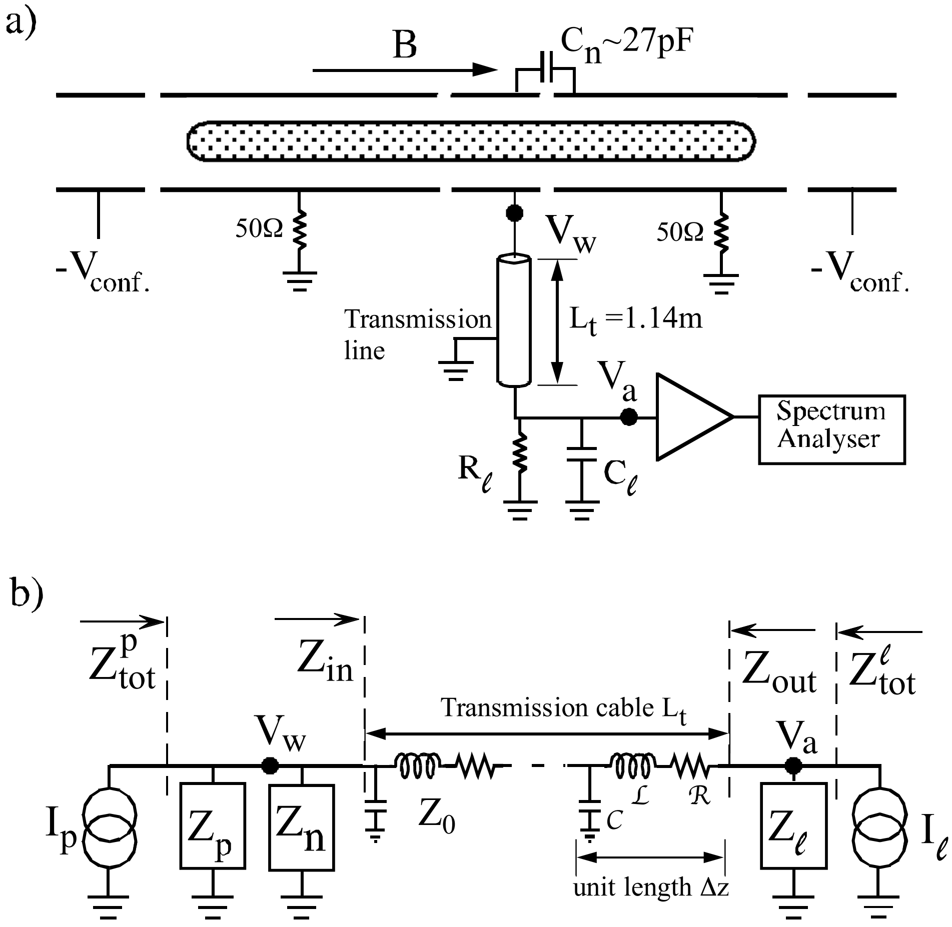

Figure 4.1: (a) Schematic diagram including transmission cable to receiver and electrode-electrode capacitance C_n. (b) Electrical circuit analogue.

of the receiver amplifier is a resistor R_ℓ=690Ω and capacitor C_ℓ=60pF in parallel. This C_ℓ only include a 40pF inherent amplifier capacitance and the cable to the machine (20pF) in this chapter. The sum of the simple capacitances of Z_n($2 \times$ 27pF∼50pF), transmission cable(80pF), and receiver amplifier Z_ℓ(60pF) adds up to the load capacitance $C_\ell \sim$ 190pF used in the simple model of Z_ℓ in figure 2.1. The voltage measured at the receiver amplifier V_a doesn't necessarily equal the voltage on the antenna V_w, due to the transmission cable resonance. This will be discussed in §4.3.

4.2 Emission Spectrum over a Broad Frequency Range

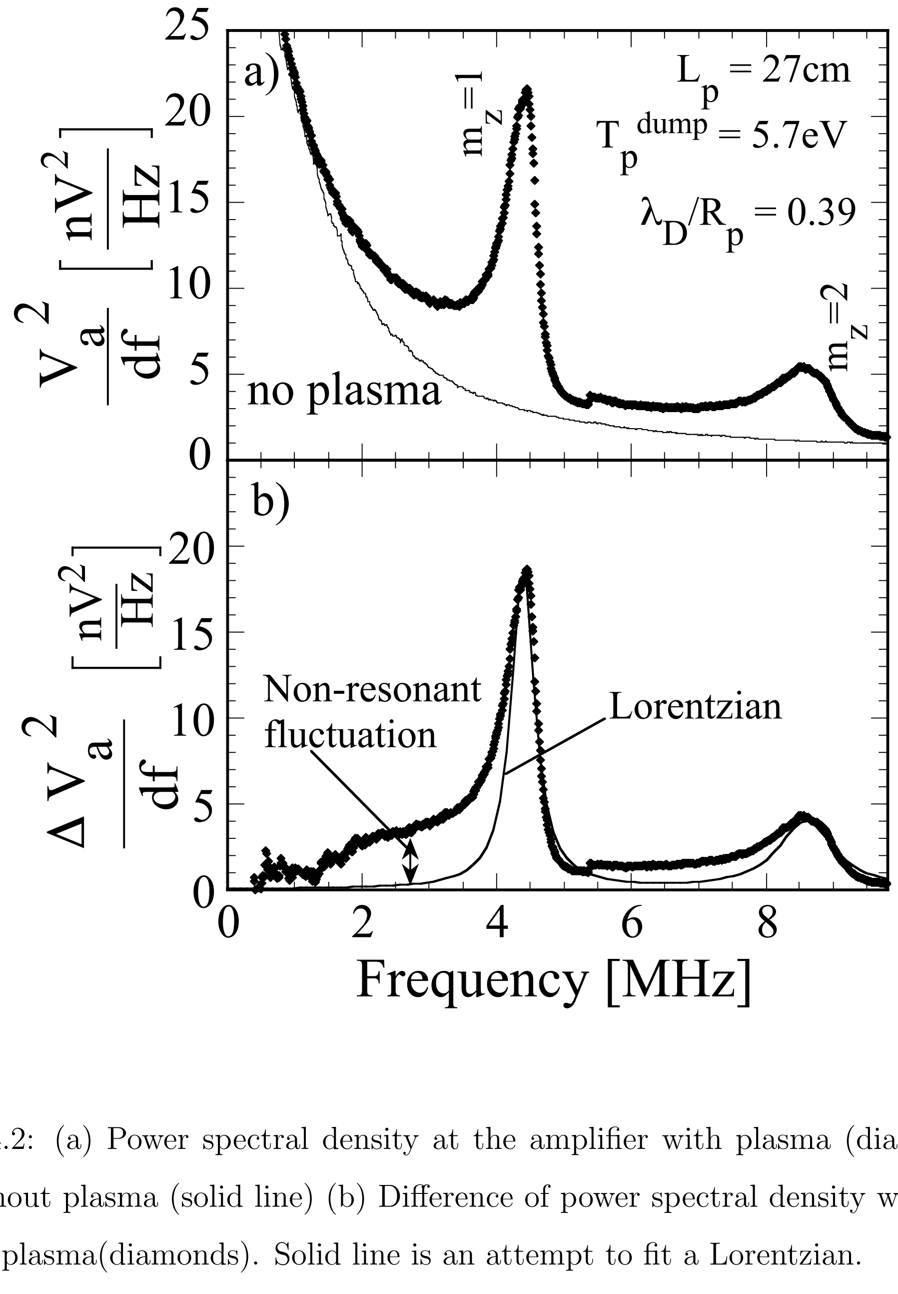

Figure 4.2: (a) Power spectral density at the amplifier with plasma (diamonds) and without plasma (solid line) (b) Difference of power spectral density with and without plasma(diamonds). Solid line is an attempt to fit a Lorentzian.

Figure 4.2(a) shows the measured emission spectrum over a frequency range encompassing two plasma modes. The mode peaks are significantly non-Lorentzian, with strong non-resonant features. The power spectrum at the receiver $\frac{V_a^2}{df}$ is shown with the plasma present (diamonds) and without plasma (solid line). Here, we used an analogue spectrum analyzer with BW=100kHz, video filter=100Hz, and scan time=0.5sec for a scan range=5MHz. This data was then averaged over 16 plasma "shots." Figure 4.2 is a combination of 2 sets of data with frequency ranges of 0.5 to 5.4MHz and 5.4 to 10MHz.

The plasma parameters obtained from "dump" measurements are $T_p = 5.7$eV, n_0=1.0×10^7cm^{-3}, $L_p = 27$cm, and R_p=1.6cm. We used the "2D Poisson solver" [DavidsonKevin] to obtain n, L_p, R_p. This is a computer program that takes the measured z-integrated charge as a function of radius and distributes the charge in z so as to consistent with the resulting potential, assuming a Maxwell distribution of particles. L_p and R_p are the positions at which the density drops to half. Wiggle heating of 5V, with frequency swept from 0.5MHz to 4MHz in 50ms, was applied 200ms prior to the measurement.

The emission attributable to the plasma is shown in Figure 4.2(b); this is the difference of the power spectral density with and without plasma. The attempt to fit the plasma noise with a Lorentzian is shown by a solid line. The plasma modes show significantly more power on the low-frequency sides of the modes.

Figure 4.2(b) shows 2 modes, corresponding to $m_z = 1$ and 2. This high temperature plasma has $\lambda_D/R_p \gtrsim 0.3$. In this high temperature regime, mode is strongly damped and broad spectrum arises in between modes. That is the simple pole model of plasma impedance Z_m^{-1} does not describe the spectral shape any longer.

4.3 Transmission Line Resonance

For frequency ranges above 5MHz, the receiving cable impedance must be treated properly. For frequencies below 5MHz, the cable mainly contributes an additional capacitance which was incorporated as part of the load. However, when the frequency becomes high enough that the length of the transmission cable is no longer small compared to the wavelength in the cable, a more complete analysis is required.

The transmission cable is modeled with repeating $\mathcal{L}, \mathcal{C}, \mathcal{R}$ components, as shown in Figure 4.1(b). $\mathcal{L}, \mathcal{C}, \mathcal{R}$ refers to the inductance, capacitance, and resistance per unit length of the cable, and bear no direct relation to the plasma model of Appendix C. We define V_{wp} as the voltage induced by the plasma on the wall side and V_{ap} as a voltage induced by the plasma, transmitted through the cable, and measured at amplifier side as shown in Figure 4.1(c). This V_{wp} and V_{ap} equals V_w and V_a respectively when thereis no load-generated noise ($I_\ell = 0$).

We calculate the transmission line voltage ratio ξ is defined as the ratio of the two voltages at the both ends of the transmission line. ξ depends on the cable impedance Z_0 ($\approx 90\Omega$), the cable length L_T and propagation constant Γ, and the receiver impedance Z_ℓ [17], as

$$\xi(\omega) \equiv \frac{V_{ap}(\omega)}{V_{wp}(\omega)} = \left| \frac{Z_\ell}{Z_\ell cosh(\Gamma L_T) + Z_0 sinh(\Gamma L_T)} \right|, \tag{4.1}$$

where

$$\Gamma \equiv \sqrt{\omega^2 \mathcal{L}\mathcal{C} + i\omega\mathcal{R}\mathcal{C}}$$

$$Z_0 \equiv \sqrt{\frac{\mathcal{R} + i\omega\mathcal{L}}{i\omega\mathcal{C}}}$$

Figure 4.3 shows the calculated $\xi(f)$ from Eq.(4.1), for 3 cases: (1) $Z_\ell = 690\Omega//60pF$ (our amplifier); (2) $90\Omega//30pF$ ($Z_0 = 90\Omega$ with 1 foot length BNC cable); (3) $50\Omega//30pF$ (popular input impedance of amplifier with BNC cable). The coax cable that connects the cylinders to the outside of the vacuum chamber is

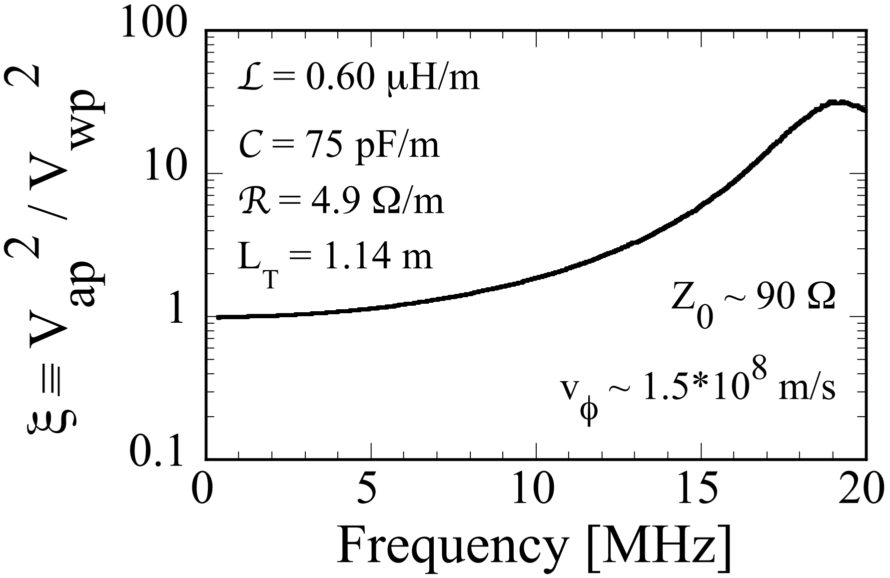

Figure 4.3: Calculated voltage V_{ap} induced by plasma on the amplifier, normalized by the voltage V_{wp} presumably induced by the plasma directly on the antenna wall versus frequency, for 3 different receiver impedances.

a hand made coax cable with 0.33mm central copper wire and 0.46cm inner diameter copper tube as a shield, insulated with an alumina tube in between. This coax is well modeled with the $\mathcal{L}, \mathcal{C}, \mathcal{R}$ parameters of Figure 4.3. These parameters were obtained by comparing the resluting calculated impedance to reflection/absorption measurements of the cable. The central copper cable itself has DC resistance of only 0.3Ω/m, so $\mathcal{R}$ presumably represents r.f. dissipation in the alumina dielectric. The impedance of our receiver $Z_\ell \sim 690//60pF$ was separately obtained by a reflection/absorption measurement.

We can see from the Figure 4.3 that the spectrum changes as we change the receiver impedance Z_ℓ. When $Z_\ell \sim Z_0 \sim 90\Omega$, ξ is flat. When $Z_\ell = 50\Omega < Z_0$, ξ decreases as the frequency goes up. When $Z_\ell = 690\Omega > Z_0$, V_{ap} is resonantly amplified by the transmission cable, causing V_{wp} to have a peak at 19MHz, with a peak gain of 6× in voltage. This transmission cable resonance is advantageous for our measurement, because the electrostatic fluctuations of plasmas have smaller spectral densities at higher frequencies.

Using a lower Z_ℓ that matches Z_0 avoids this cable resonance, but would give less signal. In order to see the difference of the signal depending on the receiver impedance, we then calculate the voltage V_{ap} that we would measure when an oscillating charge $q(\omega)$ is induced on the antenna.

The image charge $q_w = I_p/i\omega$ on the antenna wall induces a voltage V_{wp} on the amplifier as

$$\begin{aligned} V_{ap} &= \xi \; I_p \; |Z^p_{tot}| \\ &= \xi \; q_w \; i\omega \; |Z^p_{tot}| \end{aligned} \tag{4.2}$$

where

$$\begin{aligned} (Z^p_{tot})^{-1} &= Z_p^{-1} + Z_n^{-1} + Z_{in}^{-1} \\ Z_{in} &= Z_0 \left(\frac{Z_\ell cosh(\Gamma L_T) + Z_0 sinh(\Gamma L_T)}{Z_0 cosh(\Gamma L_T) + Z_\ell sinh(\Gamma L_T)} \right). \end{aligned} \tag{4.3}$$

Z^p_{tot} is a total impedance of $Z_p, Z_n, and\ Z_{in}$, that plasma current I_p sees (Figure 3.10). Z_{in} is an input impedance of the transmission cable terminated with Z_ℓ at the end [17]. The image charge induce a voltage $V_{wp} = I_p|Z^p_{tot}|$ at the antenna, then calibrated for the transmission cable by ξ.

Figure 4.4 shows the calculated voltage $|V_{ap}|$ induced on the receiver, normalized by the voltage that would have induced on single capacitance C_ℓ (that is, q_w/C_ℓ) versus frequency. This ratio $\frac{V_{ap}}{q_w/C\ell}$ is essentially the efficiency to measure the charge induced on the antenna as a voltage on the amplifier.

For 690Ω, the frequency below 2MHz is dominated by resistive load, since $f_{R_\ell C_\ell} = 1.2$MHz $R_\ell = 690\Omega$ and C_ℓ=190pF; this causes the response to fall to zero at $f = 0$. At intermediate frequencies, the behavior is determined by the capacitance and is roughly constant. For f >10MHz, V_a increases due to the cable resonance. The same calculation is plotted for R_ℓ=90Ω and 50Ω. These Z_ℓ have

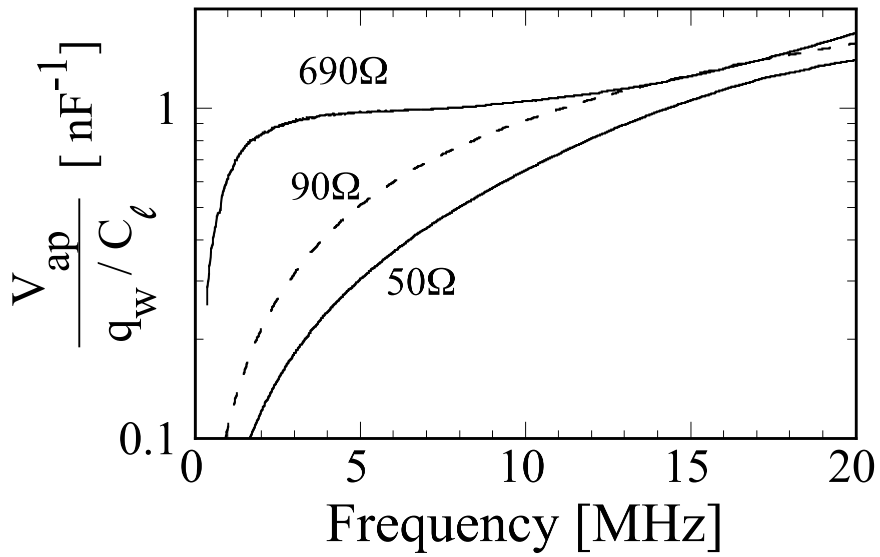

Figure 4.4: Calculated voltage V_r induced by charge q_w on receiver amplifier normalized by q_w/C_ℓ for 3 cases of Z_ℓ.

a larger resistive regime, and therefore lower gain for measuring charge on the antenna.

High receiver resistance R_ℓ gives a broader "capacitive" frequency range. Since lower C_ℓ gives higher V (=q/C) in capacitive regime, an ideal amplifier would have low C_ℓ with high R_ℓ.

In calculating the fluctuating voltage V_a, we use the same Nyquist approach as in the previous chapter. Applying the Nyquist theorem to the circuit shown in Figure 4.1(b), we get

$$\begin{aligned}\frac{V_a^2}{df}(\omega) &= \xi^2 \, \frac{I_p^2}{df} \, |Z_{tot}^p|^2 + \frac{I_\ell^2}{df} \, |Z_{tot}^\ell|^2 \\ &= 4\mathrm{k_B} T_p \, \mathrm{Re}\{Z_p^{-1}\} \, \frac{V_{ap}^2}{V_{wp}^2} \, |Z_{tot}^p|^2 + 4\mathrm{k_B} T_r \, \mathrm{Re}\{Z_\ell^{-1}\} \, |Z_{tot}^\ell|^2\end{aligned} \tag{4.4}$$

The voltage measured at amplifier V_a^2 has 2 components. 1) One is the fluctuating voltage induced by plasma current running through the total impedance seen at antenna Z_{tot}^p(see Eq (4.3)), corrected for the cable resonance volatege ratio ξ^2. 2) The other is the receiver amplifier noise current running through total impedance Z_{tot}^ℓ that the load current I_ℓ sees. Where,

$$\left(Z_{tot}^\ell\right)^{-1} = Z_\ell^{-1} + Z_{out}^{-1}$$

and, Z_{out} is an output impedance of the transmission cable terminated with $\frac{1}{1/Z_p+1/Z_n}$ at the antenna side and calculated as

$$Z_{out} = Z_0 \left(\frac{\frac{1}{1/Z_p+1/Z_n} cosh(\Gamma L_T) + Z_0 sinh(\Gamma L_T)}{Z_0 cosh(\Gamma L_T) + \frac{1}{1/Z_p+1/Z_n} sinh(\Gamma L_T)} \right). \tag{4.5}$$

4.4 Kinetic Theory Calculation of Plasma Admittance

In this chapter, we will use kinetic theory for calculating the plasma admittance Z_p^{-1}. All the quantities on the right hand side of Eq. (4.4) are independent of the plasma parameters and are measurable, except for Z_p and T_p. Therefore, we need to determine Z_p in order to determine T_p.

The following kinetic theory calculation was primarily developed by Prof. R.W. Gould [21]. An independent calculation by Prof. D.H.E. Dubin [10] was also used, giving identical spectra.

The current flowing onto an antenna cylinder in response to a plasma charge is calculated by integrating the displacement current over the surface area $A = 2\pi R_w L_a$ of the antenna. This gives

$$I = -i\omega\varepsilon_0 \int_A E_r \, dS, \tag{4.6}$$

where E_r is the radial electric field at the wall. The electrostatic potential is assumed to spatial Fourier decomposition

$$\phi(r, z) = \sum_m \phi_m(r) cos(k_z z), \quad 0 < z < Lp$$

with $k_z \equiv m\pi/L_p$, and $m \equiv m_z$; then

$$E_r = -\sum_m \phi'_m(r) cos(k_z z).$$

Eq.(4.6) can be written

$$I = -i\omega\varepsilon_0 A \sum_m \phi'_m(R_w) M_m,$$

where M_m represents the overlap of the mode m with the antenna cylinder, as

$$\begin{aligned} M_m &\equiv \frac{1}{A}\int_A cos(k_z z) dS \\ &= cos(k_z z_c)\ sin\left(\frac{k_z(z_2 - z_1)}{2}\right)\left[\frac{k_z(z_2 - z_1)}{2}\right] \\ &= \frac{1}{k_z L_a}[sin(k_z z_2) - sin(k_z z_1)] \\ &= \frac{L_p}{L_r} F_m. \end{aligned} \tag{4.7}$$

The antenna ends z_1, z_2 and the sinusoidal mode factor F_m entered the coupling coefficient $\mathcal{G}$ of Eq. (3.17). When $k_z(z_2 - z_1) \ll 1$ and the antenna is located at the end of plasma, M_m goes to unity. This M is a dimensionless "structure factor" which depends only on the location and size of the antenna cylinder in relation to the mode.

When a potential V is applied to the antenna, this excites various Fouier components ϕ_m, of magnitude

$$\phi_m(R_w) = 2VM_m.$$

Thus we can write

$$I = -i\omega\varepsilon_0 A/R_w \sum_m \chi_m(\omega) M_m^2 2V, \tag{4.8}$$

so that

$$\begin{aligned} \underline{Z_p^{-1}(\omega) = I/V} &= -i\omega 2\frac{\varepsilon_0 A}{R_w}\frac{L_w}{L_p}\sum_m \chi_m(\omega) M_m^2 \\ &\underline{= -i\omega 4\pi\varepsilon_0 \frac{L_a^2}{L_p}\sum_m \chi_m(\omega) M_m^2,} \end{aligned} \tag{4.9}$$

where $\chi_m(\omega) = -R_w\phi'_m(R_w)/\phi(R_w)$ is a dimensionless susceptibility under strong magnetic field, expressed as

$$\begin{aligned}
\chi_m(\omega) &= G_3\frac{F(\omega)+G_1}{F(\omega)+G_2}, \qquad (4.10)\\
F(\omega) &\equiv H(\omega)R_p\left[\frac{J_0'(H(\omega)R_p)}{J_0(H(\omega)R_p)}\right],\\
G_1 &\equiv k_zR_p\frac{I_0'(k_zR_w)K_0'(k_zR_p)-K_0'(k_zR_w)I_0'(k_zR_p)}{K_0'(k_zR_w)I_0(k_zR_p)-I_0'(k_zR_w)K_0(k_zR_p)},\\
G_2 &\equiv k_zR_p\frac{I_0(k_zR_w)K_0'(k_zR_p)-K_0(k_zR_w)I_0'(k_zR_p)}{K_0(k_zR_w)I_0(k_zR_p)-I_0(k_zR_w)K_0(k_zR_p)},\\
G_3 &\equiv k_zR_w\frac{K_0'(k_zR_w)I_0(k_zR_p)-I_0'(k_zR_w)K_0(k_zR_p)}{K_0(k_zR_w)I_0(k_zR_p)-I_0(k_zR_w)K_0(k_zR_p)},\\
H(\omega) &\equiv k_z\sqrt{-\varepsilon_3}, \quad \varepsilon_3 = 1-\frac{1}{k_z^2\lambda_D^2}X'(y_n),\\
y_n &= \frac{v_\phi}{\bar{v}} = \frac{1}{k_z\lambda_D}\frac{\omega}{\omega_p},
\end{aligned}$$

where $X(y_n)$ is the plasma dispersion function [normally denoted $Z(y_n)$]. This kinetic theory calculation assumes 1) the z-boundary conditions are periodic (as for k_z in an infinite length plasma), 2) the plasma has constant density out to R_p, and 3) that kinetic Landau damping is the only significant damping mechanism (e.g. electron-neutral collisions are negligible).

4.5 Experimental Spectra Fit to Theory

The measured broad spectra show stunningly close agreement with the predictions of kinetic theory. Figure 4.5 shows the voltage power spectra on the receiver amplifier.

At $T_p^{dump} = 0.7eV$, we can see up to $m_z = 7$ modes. The $m_z = 1$ mode has small spectral density because the antenna is centered on a node. As the temperature increases to 2.7eV, each mode frequency increases somewhat due to thermal pressure, the damping increases strongly due to Landau damping, and the broad inter-peak spectrum increases. At $T_p^{dump} = 5.4eV$, the modes are damped within one cycle, and the broad spectrum becomes dominant.

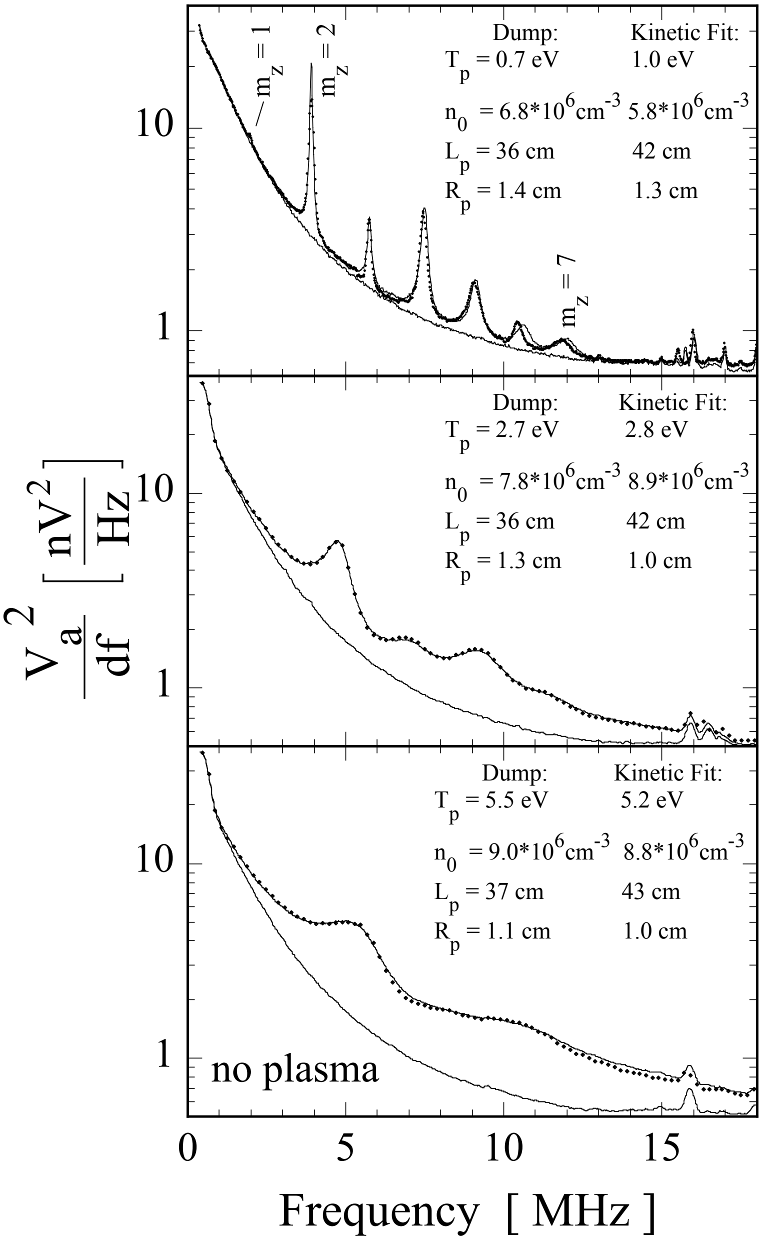

Figure 4.5: Emission spectral density on the receiver amplifier for T_p=0.7, 2.7, and 5.4eV. Lower curves are receiver noise spectra without plasma. Upper curves show kinetic theory of Eq. (4.4), …, (4.10), with T_p, n_0, L_p, R_p as fit parameters. For T_p=2.7 and 5.5 eV, only 10% of the measured data are shown in dots to make the fit curve visible.

After injection, we applied a wiggle heating 200ms prior to the spectrum measurement, in order to change the temperature $T_p = 2.7$eV (and 5.4eV). All of the transmission cables that are connected to the cylinders are terminated with 50Ω, except for the one connected to the antenna.

Lower lines on each spectrum are the fluctuation spectrum without plasma, representing receiver noise.

For T_p^{dump}=2.7 and 5.4eV, we used spectrum analyzer with Band Width(BW)=300kHz, video filter=100Hz, scan time=0.5s, and scan range=20MHz. For T_p^{dump}=0.7eV, we used BW=100kHz and took 4 separate scan over 5MHz to get 0 to 18MHz spectrum. Spectral density at each frequency was averaged over 16 shot. For T_p=2.7 and 5.5 eV, 10% of the measured data are shown in dots to make the fit curves visible.

Now we explain how the temperature was determined through fit to kinetic theory. We rewrite the Eq. (4.4) to make Z_p^{-1} more explicitely visible:

$$\begin{aligned}\frac{V_a}{df}(\omega) =& 4\mathrm{k_B}\mathbf{T_p}\mathrm{Re}\{\mathbf{Z_p^{-1}}\}\xi^2|\mathbf{Z_p^{-1}} + Z_n^{-1} + Z_{in}^{-1}|^{-2} \\ &+ \frac{I_\ell^2}{df}\mathrm{Re}\{Z_\ell^{-1}\}\left| Z_\ell^{-1} + Z_0^{-1}\left(\frac{\frac{1}{\mathbf{Z_p^{-1}}+Z_n^{-1}}cosh(\Gamma L_T) + Z_0 sinh(\Gamma L_T)}{Z_0 cosh(\Gamma L_T) + \frac{1}{\mathbf{Z_p^{-1}}+Z_n^{-1}}sinh(\Gamma L_T)}\right)^{-1}\right|^{-2}\end{aligned} \tag{4.11}$$

We directly measure all quantities on the right hand side such as Z_ℓ, ξ, Z_n^{-1}, Z_{in}^{-1}, Γ, L_T, Z_0, $\frac{I_\ell^2}{df}$, except for T_p and Z_p. The measured spectrum without plasma was used to calculate the receiver amplifier noise $\frac{I_r^2}{df}$ in Eq(4.4). Z_p is calculated by the kinetic theory and has 4 parameters, T_p, n_0, L_p, R_p.

Thus, the right hand side of Eq. (4.11) has 4 parameters, and fitting to the measured spectral data determines all 4 parameters. We used a Fortran program to calculate the spectrum for any given set of 4 parameters, and fit to the measured spectra. The SLATEC Fitting routine sNLS1 was used to carry out the 4 parameter fit. sNLS1 minimizes the sum of the squares of M (number of data points) nonlinear functions in N variables by a modification of the Levenberg-Marquadt algorithm.

When the modes were very weakly damped, as for T_p=0.7eV, the fitting routine did not readily converge to the correct answer, and we needed to start with the parameters that were close to "right" ones. In contrast, the fit converged easily for spectrum with strong damping of the modes.

At all 3 temperatures in Figure 4.5, the kinetic theory calculates the emission spectrum so well that allowed us to determine the plasma parameters, T_p, n_0, L_p, and R_p, from the broad emission spectrum. This means that we can determine the all 4 plasma parameters with an emission data digitized over $\frac{1}{2\pi\gamma_{min.}}$ sec. Here, $\gamma_{min.}$ is the damping of the mode that has the minimum damping of all m_z.

One oddity is that L_p^{kin} obtained from the fit is consistently 17% higher than L_p^{dump} obtained from the Poisson solver. This is due to "end effect" on Landau damping in finite length system, and is discussed in more detail in Sec. 4.7.

Here, we calculate the charge number fluctuation spectrum $\frac{\delta N_w^2}{df}$ from the measured $\frac{V_a^2}{df}$ on the antenna. All the experimental complications like receiver noise spectrum $\frac{V_a^2(f)}{df}$ are removed from $\frac{\delta N_w^2}{df}$, so it is easier to compare with theory directly.

We calibrate the $\frac{\delta N_w^2}{df}$ from$\frac{V_a^2}{df}$ as follows.

$$\begin{aligned}\frac{\delta N_w^2}{df} =& \frac{I_p^2}{df}\frac{1}{\omega^2 e^2}\\ =& \frac{\Delta V_a^2}{df}\xi^{-2}|Z_{tot}^p|^{-2}\frac{1}{\omega^2 e^2},\end{aligned} \tag{4.12}$$

where $\frac{\Delta V_a}{df}$ is a difference of the voltage spectrum $\frac{V_a^2}{df}$ with and without plasma. $\frac{\Delta V_a}{df}$ is corrected for the transmission line resonance ξ, converted to the current by $|Z_{tot}^p|^{-2}$ then finally divided by $\omega^2 e^2$ to obtain charge fluctuation $\frac{\delta N_w^2}{df}$. $|Z_{tot}^p|^{-2}$ includes Z_p^{-1}, and we used the Z_p^{-1} that was obtained by the previous fit.

Figure 4.6 displays the spectrum of $\frac{\delta N_w^2}{df}$ for the thermal emission measurements of Figure 4.5. At 0.7eV, we see that measurement and theory agrees within 30% over a wide range in frequency, encompassing 7 modes; and that the dynamic range for the amplitude is about three orders of magnitude. Moreover, correspondence

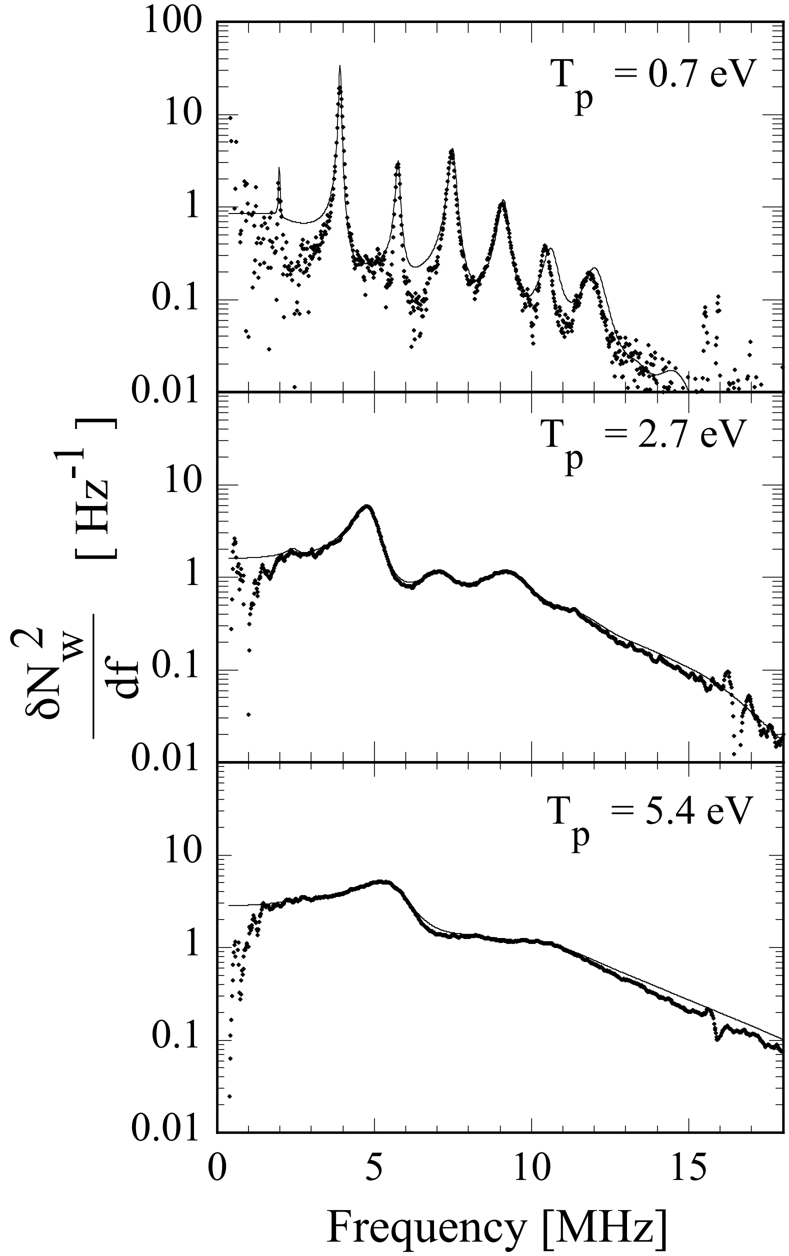

Figure 4.6: Charge number fluctuation spectra for the data of Figure 4.5, with kinetic theory fits.

is obtained at all temperatures, here ranging over a factor 8.

Our detection electronics loses gain below 1.5MHz, because the amplifier becomes resistive below$f_{RC} = \frac{1}{2\pi RC}$ ~1.2MHz, with gain proportional to frequency squared (as described above).

4.6 Effect of the 50Ω Termination of the Cable

The received emission spectrum is slightly enhanced above 10MHz when cables from the neighboring sectors are shorted to ground rather than terminated with 50Ω. We note this mainly because grounded cylinders are the norm in these traps. Figure 4.7 shows the spectrum with shorted transmission cables connected to the neighboring wall electrodes. This plasma is created in the same way as the $T_p =$ 2.7eV plasma in Figure 4.5 and 4.6; but the received specrum from 10-15MHz is up tp 4× larger than kinetic theory, which closely modeled measurements with 50Ω terminations.

The measured broad fluctuation is larger than kinetic theory calculation above 10MHz shown in Figure 4.7(b) This extra noise is probably due to fluctuating voltages on neighboring cylinders coupling into the antenna. The neighboring cylinder cable resonance also enhanced the receiver noise near 14MHz as shown in Figure 4.7(a).

Both the extra noise of plasma above 10MHz, and the resonant receiver noise at 14MHz are avoided by terminating the cables with 50Ω in Figures 4.5(b) and 4.6(b).

We note that 90Ω would better matche the cable impedance Z_0, and would therefore terminate the cable resonance better than 50Ω. However, the resistive load damping of the mode is proportional to the resistance of the termination. 50Ω was at the level that broadens the cable resonance enough, and yet keeps the resistive damping lower.

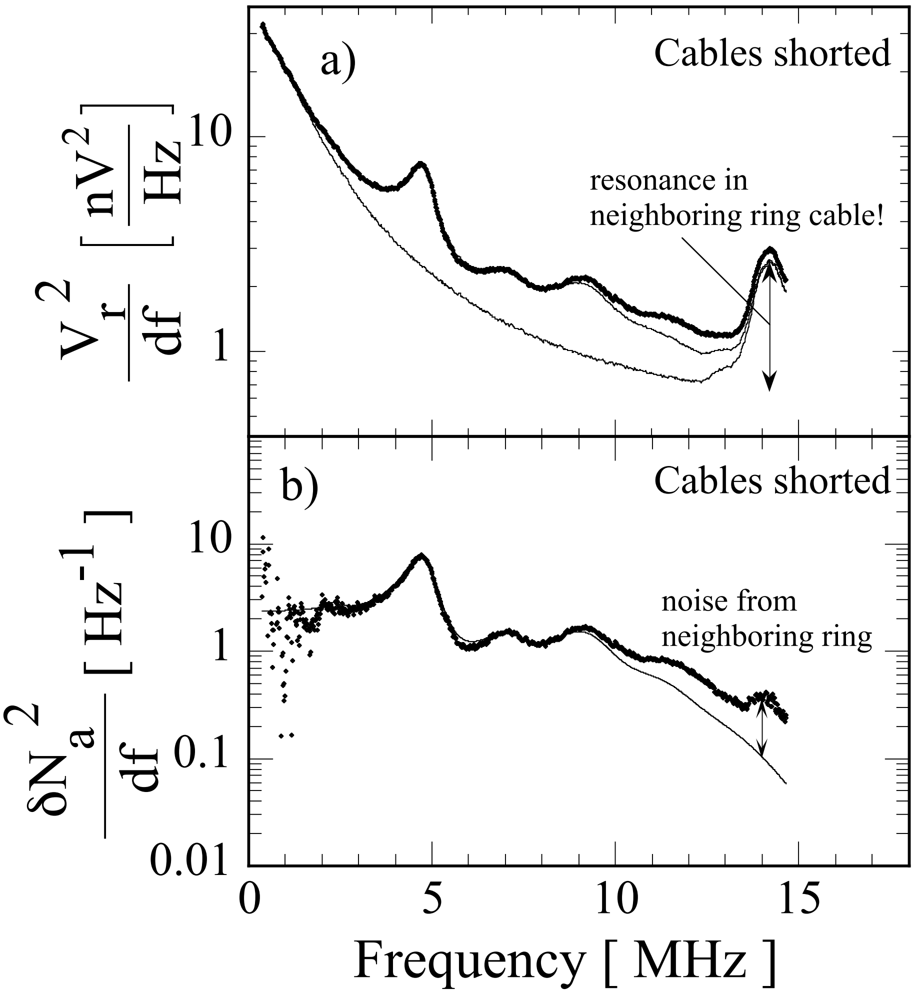

Figure 4.7: (a) Emission spectral density with neighboring electrode cables shorted to ground. (b) Equivalent charge number fluctuation.

4.7 Broad Spectrum Temperature Diagnostic

This broad spectrum gives an accurate diagnostic of the plasma temperature T_p (and also diagnoses n_0, R_p, and L_p) for plasma with $L_p \gtrsim 20$. For shorter plasmas, the method becomes inaccurate because kinetic theory overestimates the actual Landau damping in finite length plasmas.

Figure 4.8 displays the plasma temperature T_p^{kin} obtained from the emission spectra fitted to the kinetic theory calculation, versus the plasma temperature T_p^{dump} measured by dumping the plasma. Transmission cables were terminated with 50Ω for solid diamonds(◆) and were shorted for all the open symbols.

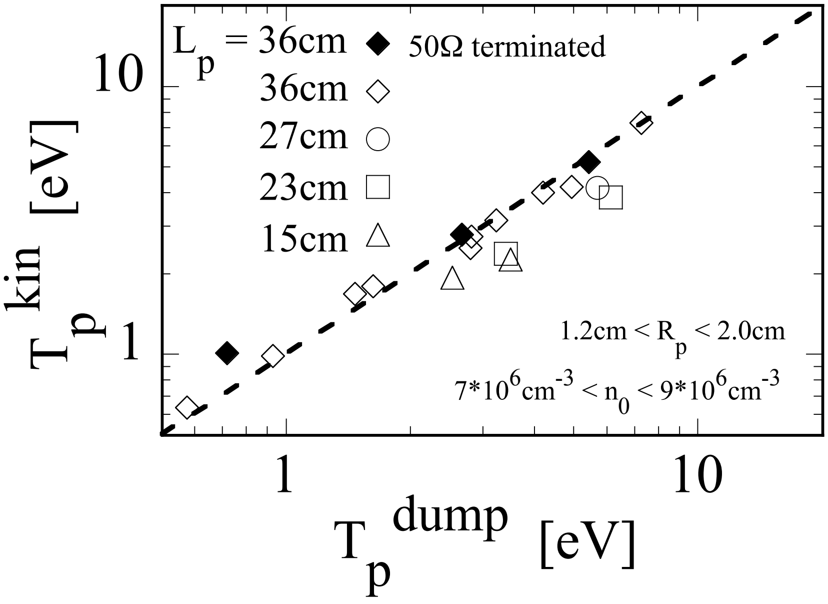

Figure 4.8: Temperature obtained with kinetic theory versus temperature obtained with dump. Length varies from 15 to 36cm.

The fit gives accurate temperatures for 36cm plasmas, even when the cables were not terminated with 50Ω. This is because the spectrum below 10MHz dominates, and the fit is not significantly affected by the transmission cable resonance above 10MHz. For shorter plasmas, T_p^{kin} is systematically lower thanT_p^{dump}. The kinetic theory assumes periodic z-boundary condition, and therefore significantly overestimates the Landau damping for finite length plasmas.

Fitting the kinetic theory to broad emission spectra determines the plasma temperature T_p, as well as n_0, R_p, and L_p. We find that T_p is accurately determined for long plasmas (with $L_p/R_p \gtrsim 20$); but that the fit is less satisfactory for shorter plasmas, because kinetic theory with periodic z-boundaries does not properly model Landau damping in finite-length plasmas.

Figure 4.9 is an example of such a case, where the kinetic theory at the actual T_p predicts much broader peaks (stronger damping) than the measured peak width. The solid line is a kinetic theory calculation at the actual plasma temperature, showing $\gamma \sim 2\times$ too large. The dashed line is a best "fit", giving temperatures about 2× too small. This fit also gives $n_0 R_p^2$ about 1.3× too large, and N_{tot} about 1.5× too large.

That is kinetic theory overestimates the Landau damping by a factor of 2 for this length. The fitting routine matches the damping by lowering the temperature.

Landau damping is predicted to depend on the mode phase velocity $v_\phi \equiv \omega/k_z$; but the definition of k_z for finite length plasmas is problematical. We define an "effective wave number" k_z^{eff} as that which gives the measured mode frequency ω_m in linear(infinite-length) wave theory. This k_z^{eff} is then used to calculate v_ϕ, as $v_\phi = \omega_m/k_z^{eff}$. This k_z^{eff} is typically 20% lower than $\frac{m\pi}{L_p}$, as was first discussed by Spencer [29].

Figure 4.10 shows the predicted and observed damping γ (normalized by mode frequency ω_m) versus thermal velocity $\bar{v}^2$ over phase velocity $v_\phi^2 \equiv (\omega/k_z^{eff})^2$ squared. The symbols show experimental data for various L_p. Here, γ is the half-width at half-maximum of the δN^2 spectrum, measured on the higher side of the mode. We picked the mode that has the largest amplitude out of the spectra that were used for Figure 4.8 in order to determine γ and ω_m. For long plasmas,

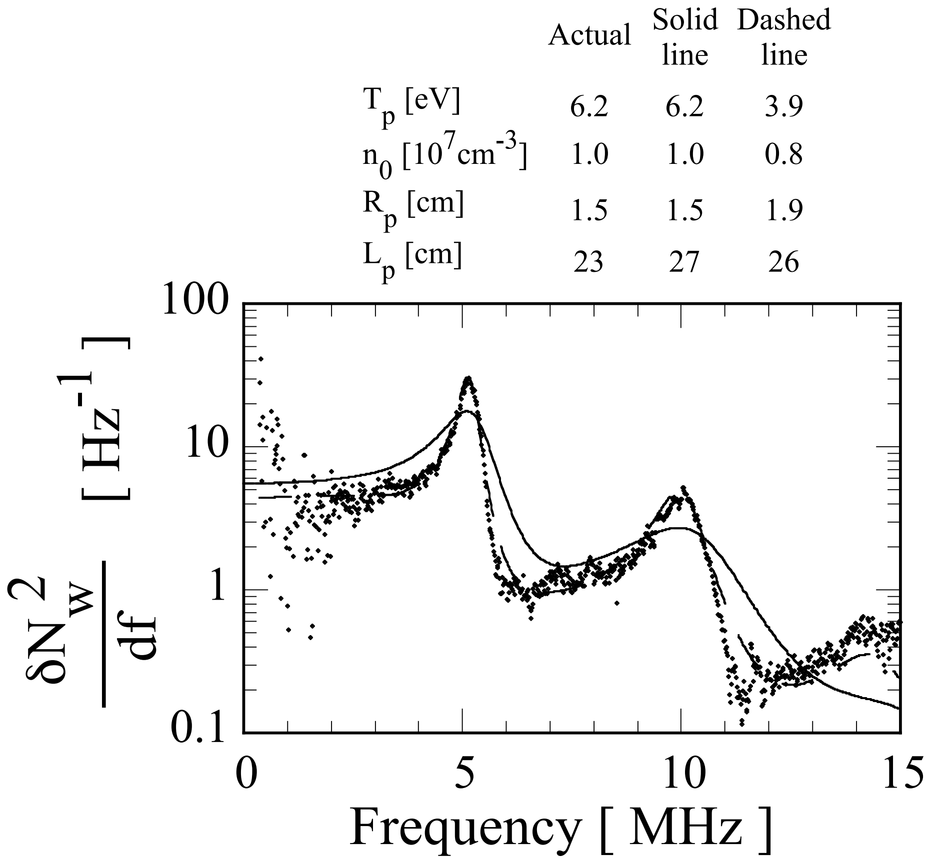

	Actual	Solid line	Dashed line
T_p [eV]	6.2	6.2	3.9
n_0 [10^7cm^{-3}]	1.0	1.0	0.8
R_p [cm]	1.5	1.5	1.9
L_p [cm]	23	27	26

Figure 4.9: Effects of overestimated landam damping in kinetic theory for damping and Landau damping for shorter (L_p=23cm) plasma. Solid line is a kinetic theory calculation at the actual T_p=6.2eV, using L_p^k=27cm to match the mode frequencies. Broken line is a kinetic theory fit, giving T_p^{kin}=3.9eV with compensating errors in n_0, L_p, R_p.

agreement between theory and experiment is quite close; for short plasmas theory predicts larger damping than is observed.

In the theory, $\frac{\bar{v}^2}{v_\phi^2}$ tells where the wave phase velocity is located in the velocity distribution, and thus determines the Landau damping. For shorter plasmas, damping is systematically low or else, k_z^{eff} is low compared to the theory. Clearly, end effects play a substantial role for short plasmas. As an extreme example,

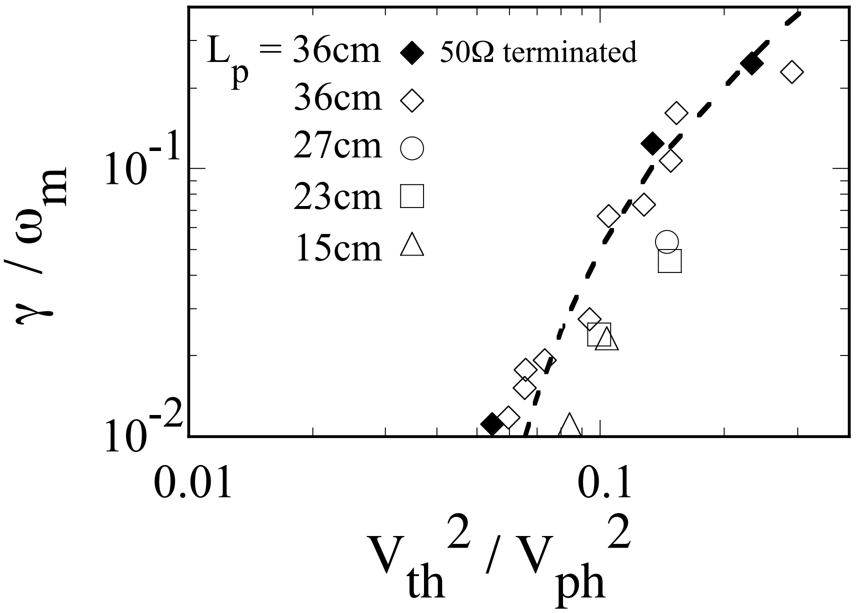

Figure 4.10: Damping γ normalized by the mode frequency ω_m versus $(\bar{v}/v_\phi)^2$

a football-shaped plasmas in a harmonic potential theoretically has no damping for modes corresponding to m_z =1 and 2 [9]. Here, no "adjustment" of k_z in infinite-length theory is likely to eliminate the damping.

Overall, our 4 parameter fit to theory determines T_p, n, L_p, R_p within 30% accuracy for the long plasmas where kinetic theory calculates the damping correctly. For short plasmas, the fit temperature deviates by 50% because the damping differs from theory by up to 5×.

4.8 Total Fluctuation Temperature Diagnostic

All errors associated with the details of the spectrum can be avoided by looking at the total frequency-integrated fluctuation level δN_w^2 induced on the wall antenna. Thermodynamic theory[Dubin,O'Neil] calculates δN_w^2 for any given T_p, n_0, R_p, and geometry. This thermodynamic argument is more general than kinetic theory, in the sense that it doesn't invoke the shape of the spectrum.

The work of Dubin resulted in

$$\frac{\delta N_w^2}{N_w} = \frac{4\lambda_D^2 L_a}{R_p^2 L_p} \sum_{n=1} M_m^2 \frac{-\hat{k}_z\ I_0(k_z R_p)\ I_1(\hat{k}_z R_p) + k_z\ I_0(\hat{k}_z R_p)\ I_1(k_z R_p)}{I_0(k_z R_w)\ D}, \tag{4.13}$$

with

$$\begin{aligned} D \equiv{}& \hat{k}_z\ I_1(\hat{k}_z R_p)\big\{\ I_0(k_z R_p)\ K_0(k_z R_w) - I_0(k_z R_w)\ K_0(k_z R_p)\ \big\} \\ &-k_z\ I_0(\hat{k}_z R_p)\big\{\ I_1(k_z R_p)\ K_0(k_z R_w) + I_0(k_z R_w)\ K_1(k_z R_p)\ \big\}, \\ \hat{k}_z^{\,2} \equiv{}& k^2 + \frac{1}{\lambda_D^2}, \quad \text{and} \quad \lambda_D^2 \equiv \frac{\mathrm{k_B} T_p}{4\pi n_0 e^2}, \end{aligned}$$

Here, δN_w^2 is normalized by the total number of the electrons N_w inside the antenna region.

This rather complicated function is well approximated by a simpler form,

$$\frac{\delta N_w^2}{N_w} \cong \frac{\alpha_1}{1 + \alpha_2 (\frac{R_p}{\lambda_D})^2}. \tag{4.14}$$

This form shows that the fluctuation level is a constant in the high temperature limit, ($R_p/\lambda_D \ll 1$), and is proportional to the temperature at low temperatures ($R_p/\lambda_D \gg 1$).

In the limit $T_p \to \infty$, we obtain

$$\begin{aligned} \frac{\delta N_w^2}{N_w} &= \alpha_1 \\ &= 2\frac{L_a}{L_p} \sum_{n=1} M_m^2 \frac{I_0^2(k_z R_p) - I_1^2(k_z R_p)}{I_0^2(k_z R_w)} \\ &\to 1 - \frac{L_a}{L_p} \quad \text{for large} \frac{L_a}{R_w} \\ &\approx 0.79 \quad \text{for our geometry.} \end{aligned} \tag{4.15}$$

This represents the uncorrelated density fluctuations of the ideal gas in a cylinder. This limit was simulated and compared to experiments in Ref [34].

One caution is that the number of image charges on the antenna does not exactly equal the number of plasma charges with $z_1 < z < z_2$, because some of the electric field from the charge near the end of the antenna “leaks out” and terminates elsewhere on the wall. Thus, the ideal gas analogy is only rigorous in the limit of $\frac{L_a}{R_w} \gg 1$. In our case, $\frac{L_a}{R_w} = 2$ is not large enough to use this simple form.

In the low temperature limit where $k\lambda_D \ll 1$,

$$\begin{aligned}\frac{\delta N_w^2}{N_w} &= \frac{\alpha_1}{\alpha_2}\left(\frac{\lambda_D}{R_p}\right)^2 \\ &= 4\frac{L_a}{L_p}\left(\frac{\lambda_D}{R_p}\right)^2 \sum_{n=1} M_m^2 \frac{I_0(k_z R_p)}{I_0(k_z R_w)} \frac{1}{-I_0(k_z R_p)K_0(k_z R_w) + K_0(k_z R_p)I_0(k_z R_w)} \\ &\rightarrow \frac{1 - L_a/L_p}{\frac{1}{2}\ln(\frac{R_w}{R_p})}\left(\frac{\lambda_D}{R_p}\right)^2 \quad \text{for large}\frac{L_a}{R_w}.\end{aligned} \tag{4.16}$$

Therefore

$$\begin{aligned}\alpha_2 =& \frac{1}{2}\ln\left(\frac{R_w}{R_p}\right) \quad \text{for large}\frac{L_a}{R_w} \\ &\approx 0.54 \quad \text{for our geometry.}\end{aligned} \tag{4.17}$$

As the temperature decreases, Debye shielding supress the random particle fluctuations. At low temperatures, collective effects become dominant, and the total fluctuation is propotional to $\mathrm{k_B}T$.

Figure 4.11 shows the predicted and measured total fluctuation level versus temperature T_p or λ_D. Close agreement is obtained over a range of 10 in T_p. The solid line is the thermodynamic calculation of Eq. (4.13) using the (measured) parameters shown.

Experimental points(diamonds) were obtained by first calculating $\frac{\delta N_r}{df}$ from Eq. (4.12), using the same spectra in Figure 4.5 and Figure 4.6 and then integrated $\frac{\delta N_r}{df}$ from 0 to 18MHz, with 2 assumptions. First, we assumed $|Z_p| \gg |Z_\ell|$ so that $\frac{1}{Z_p}$ becomes negligible, allowing us to calculate δN_w without using kinetic theory calculation of Z_p. This is a good assumption except for the frequencies near a very weakly damped mode. For example, the minimum $Z_p(\sim 1200\Omega)$ of Figure 4.5 is given at the peak of the $m_z = 2$ mode for T=0.7eV, which is still larger than

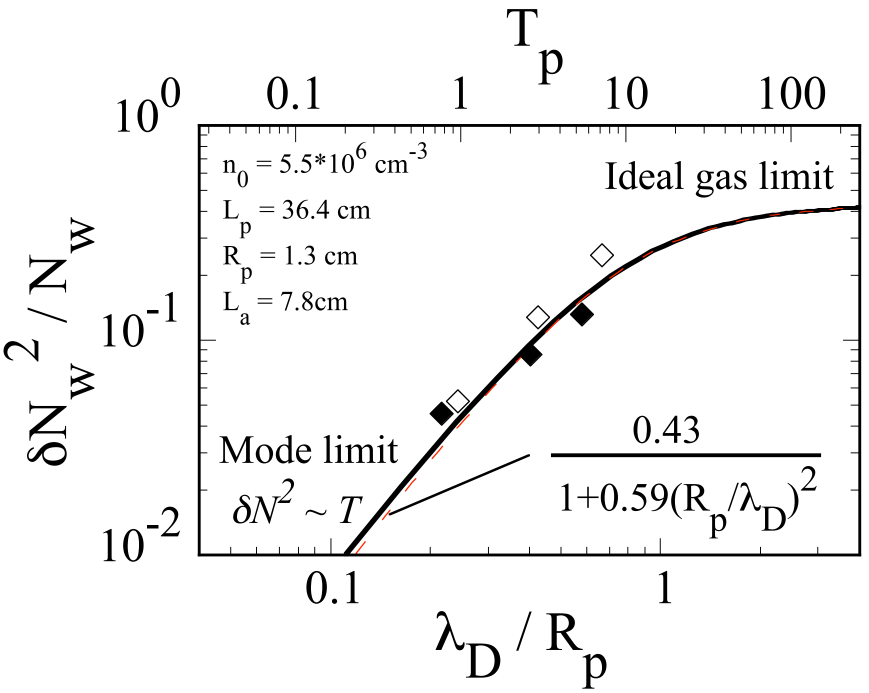

Figure 4.11: Total fluctuation square normalized by total number versus Debye length normalized by the Radius of the plasma. Solid line is the result of thermodynamic argument. Broken line is the plot of approximated form. Solid diamonds are measured data with transmission cables terminated with 50Ω and open diamonds are with shorted cables.

Z_ℓ. Secondly, we also assumed that below 2MHz, the fluctuation spectral density is flat with the value at 2MHz. This is required since our receiver loses gain below 2MHz, as the input impedance becomes resistive rather than capacitive. N_w is obtained by $N_w = N_{tot}L_a/L_p$, with N_{tot} and L_p determined by a dump measurement. Integrating up to 18MHz is sufficient, since $\frac{\delta N_w^2}{df N_w} < 10^{-8}$ at 18MHz.

The measured total fluctuations with properly terminated cables(◆) are within 20% agreement with calculation of the thermodynamic argument. The measured fluctuations with shorted cables still show fair agreement with despite the fact that the spectrum has extra fluctuation above 10MHz. For example, for the open diamond at $\lambda/R_p = 0.67$, shorted cables give a 20% increase in δN^2 above 10MHz.

The measured total fluctuation compared to the theory line of Eq. (4.13) determines the temperature of the plasma. This total fluctuation serves as a "robust" temperature diagnostic, because this method does not depend on the shape of the spectrum. However, R_p, n_0 and L_p need to be pre-determined in order to calculate the predicted total fluctuation.

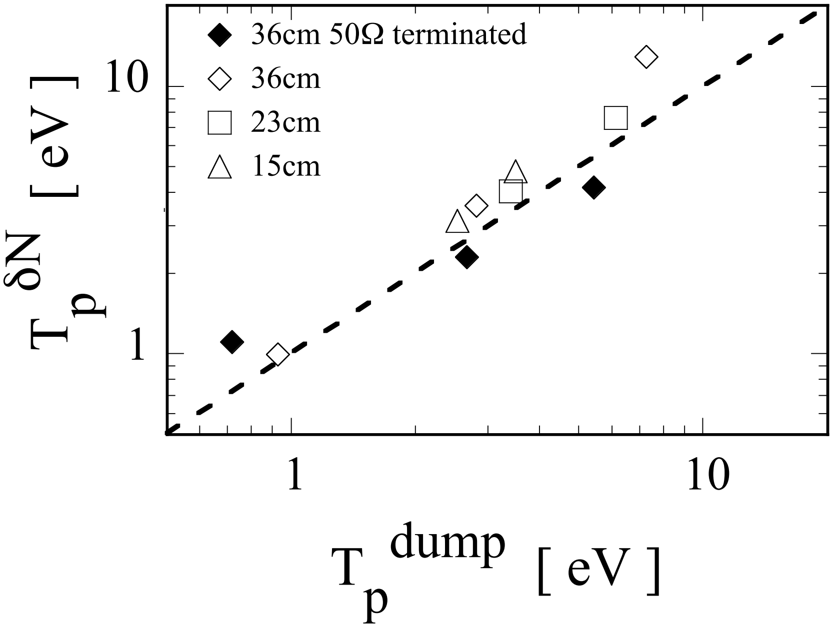

Figure 4.12: Temperature obtained from measured total fluctuation, compared with thermodynamic argument versus temperature obtained with dump. Length varies from 15 to 36cm. All the transmission cables that are connected to cylinders except for the one connected to the antenna were terminated with 50Ω for solid diamonds. The same cylinders were shorted for open symbols.

Figure 4.12 shows the temperature $T_p^{\delta N}$ of the plasma obtained from the measured total fluctuation, versus T_p^{dump}. Solid symbols are data taken with the properly terminated cables. Open symbols are plasmas with shorted cables. Open symbols estimate $T_p^{\delta N}$ consistently higher, because of the extra fluctuations. Nevertheless, this temperature diagnostics determines temperature within 50% accuracy and is independent of the form of the damping.

The charge number spectrum needs to be calibrated at each frequency and measuring the root-mean-square voltage with broad frequency(0 to 18 MHz) would not give the right total number fluctuation level.

5

Summary

We have developed three different non-perturbative strategies to determine the plasma temperature.

The first method focuses on the spectrum near a mode, and approximates Z_p^{-1} with a simple pole. This Z_p doesn't presume any particular cause of the damping, other than that it is weak. This diagnostic determines $T_p, T_\ell, \omega_m, \gamma_m$, and $\mathcal{G}$ from the spectrum. This method has proven to be fairly robust in a "quiet" plasma environment. However, we note that each mode represents 1 degree of freedom out of 10^9, and so it could easily be excited by an external signal (e.g. noise on a pulser) at the mode frequency. The second method utilizes the emission spectrum over a broad frequency range, fitting it to kinetic theory. Kinetic theory implicitly assumes that Landau damping is the only damping mechanism, and neglects end correcion to this damping. This theory matches the measured spectra extremely well, if the temperature is large enough that Landau damping is dominant, and if the plasma is long compared to the radius. This diagnostic determines all 4 fitting parameters, giving T_p, n_0, k_z, R_p.

Third method utilizes the total frequency-integrated number fluctuation, and requires prior knowledge of n_0, L_p, R_p. The frecuency integral requires a complete spectrum which is corrected for cable resonance. Comparison with a thermodynamic calculation determines the plasma temperature, so no assumptions are made as to the form of damping.

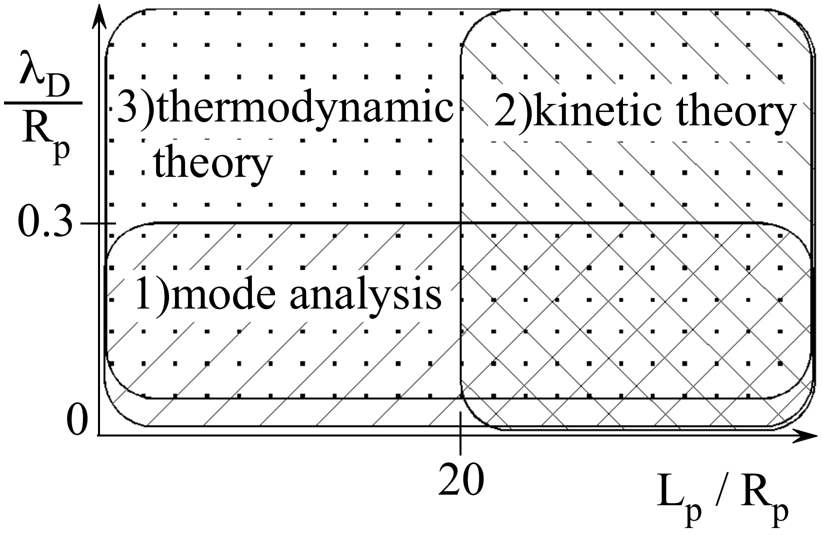

Figure 5.1: The plasma regime that 3 methods works.

Figure 5.1 summarizes the plasma regimes for which each method works. As long as the chosen mode is weakly damped, the first method is robust, and a single emission spectrum determines the temperature. When the temperature is high enough that the mode spectrum deviates from a Lorentzian, one can use kinetic theory calculation if plasma is long. For short plasmas at high temperatures, one can use the thermodynamics to calculate the total fluctuation; but this requires the separete determination of n_0, L_p, R_p.

Appendix A

Spectrum Analyzer

Many spectral concepts are subtle (or ambiguous in general usage), so we begin with an overview of spectral analysis.

Figure A.1 shows a cartoon of the block diagram of an analogue spectrum analyzer (HP 141T/8553B) [16, 23]. Digital FFT analysis will be continued in §3.5.1. Voltage signal $x(t)$ is applied to the 50Ω input and filtered through a band pass filter. Both the center frequency ω_0 and the bandwidth BW of the filter are adjustable. Then, an envelope detector together with a $1/\sqrt{2}$ calibrater obtains

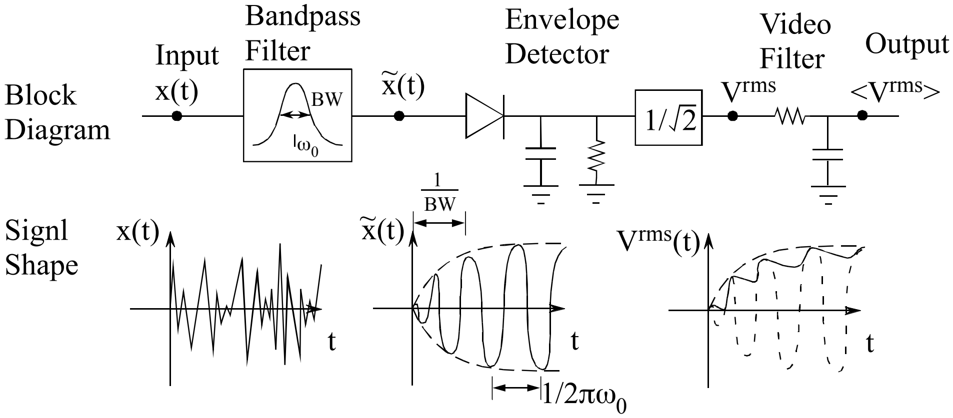

Figure A.1: Block diagram of how the spectrum analyzer process the input signal(top) and the cartoon of the signal shape(bottom).

the root-mean-square-voltage V^{rms} over the BW centered at ω_0 . In this thesis, we use the word “power” as synonymous to “squared;” the voltage or current squared is proportional to the power.

It takes about $\frac{1}{BW}$sec for the envelope of the filtered signal to reach a stationary value. For example, if we turn on a sinusoidal wave with amplitude A_o at $t = 0$, the envelope relaxes towards A_o with time constant $\frac{1}{BW}$. We can further average this power output with a video filter circuit to obtain $< V^{rms} >$. The video filter bandwidth Δf_{video} is a reciprocal of the video filtration time. The maximum of $\frac{1}{BW}$ or $\frac{1}{f_{video}}$ gives the overall response time τ_{spe} of the spectrum analyzer.

The spectrum analyzer can be operated in 2 different regimes, namely,
power measurement mode or,
power spectral density measurement mode.
These 2 modes can be selected by the choice of BW and it’s defference is explained in Figure A.2. A) chooses the BW to be broad enough to cover the whole spectrum of signal, and the peak amplitude of the output of the spectrum analyzer is the total power of the input signal. This is illustrated in Figure A.2(a). The transmission spectra of Figure 3.4(a), (b) is operated in this regime. input signal

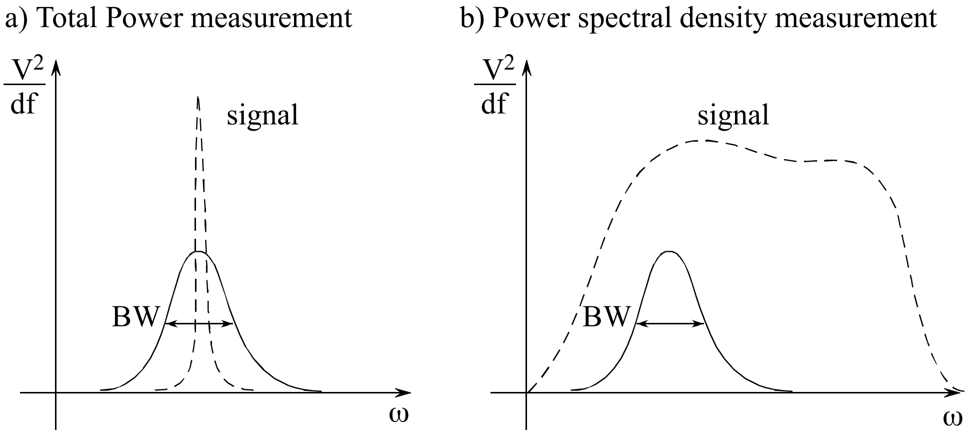

Figure A.2: Illustration of the 2 operation modes of spectrum analyzer.

is essentially a delta function, so changing the BW will not change the output power. B) chooses the BW to be narrow enough to resolve the spectrum of signal, shown in FigureA.2(b). We define the power spectral density $\frac{V^2}{df}(f)$ as the power in a unit frequency band width [Hz] centered at frequency f and measured as $\frac{V^2}{df}(f) \equiv \frac{(V^{rms})^2}{BW}$, which is really a power spectral density averaged over BW.

In dealing with random signal with a Gausian Amplitude distribution, we need to be a little careful with the power amplitude calibration. HP8553B assumes that the root mean square of the signal is $\frac{1}{\sqrt{2}} = 0.707$ of the peak envelope amplitude, which is true for stationary sinusoidal wave. However, for a random $x(t)$ with a Gaussian amplitude distribution, the output of the envelope detector is the Rayleigh-distributed envelope. The mean value of the Rayleigh-distributed noise is 0.886 of the peak envelope amplitude. Therefore output of the Spectrum analyzer is factor of 0.798 low and need to be calibrated.

In order to obtain the spectrum, we sweep the center frequency ω_0 of the band pass filter. The time it takes to sweep over BW should be longer than τ_{spe}, so that the spectrum analyzer has time to reach the full amplitude. This means that wider BW allows us to sweep faster, but we also need to make sure that BW is narrow enough to resolve the spectrum. For example, If we want to measure the spectrum over a 5MHz span with BW=100kHz and f_{video}=100Hz, the scan rate need to be less than 10MHz/s. This leads to 0.5 second total scan time over 5MHz scan. This total scan time is marginally OK in EV and perfectly fine in IV because the plasma evolves in the order of 1 second, or 100second in EV and IV respectively.

The output of the spectrum analyzer is recorded digitally as a function of frequency.

Appendix B

Power Spectral Density of Damped Harmonic Oscillator

A plasma mode is analogous to a damped harmonic oscillator. Here, we will discuss the significance of the power spectral density through the example of a damped harmonic oscillator [5].

First, consider a case that the excitation of damped oscillator takes place only once at t=0 as shown in Figure(a). The resulting impedance response $h(t)$ oscillates with frequency ω_0, and is damped at a rate γ. $h(t)$ has finite square integral

$$\begin{aligned} \int_{-\infty}^{\infty} h^2(t)\ dt &= \frac{\omega_0^2 + 3\gamma^2 - 2\gamma\omega_0}{4\gamma(\gamma^2 + \omega_0^2)} \\ &\sim \frac{h_0^2}{4\gamma} \quad \text{when } \gamma \ll \omega_0. \end{aligned} \tag{B.1}$$

This square integral is proportional to it's energy.

The Fourier transform $H(\omega)$ of $h(t)$ defined as

$$\begin{aligned} H(\omega) &\equiv \int_{-\infty}^{\infty} h(t)\ e^{-i\omega t} \\ &= \frac{h_0}{2}\left[\frac{1}{\gamma + i(\omega - \omega_0)} + \frac{1}{\gamma + i(\omega + \omega_0)}\right], \end{aligned} \tag{B.2}$$

and the "Energy spectrum" $|H(\omega)|^2$ is

$$|H(\omega)|^2 \equiv H(\omega)H^*(\omega). \tag{B.3}$$

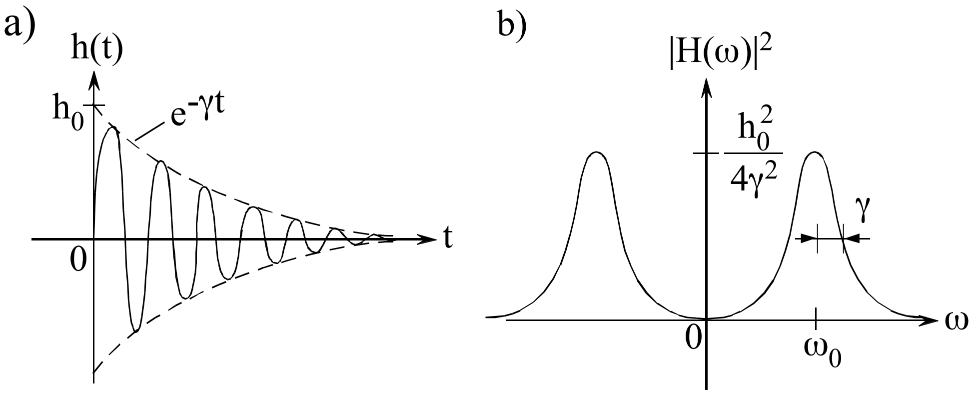

Figure B.1: Signal shape of a single excitation of damped harmonic oscillator in (a) real time space and (b) frequency space.

$|H(\omega)|$ has a Lorentzin spectral shape with amplitude $\frac{h_0^2}{4\gamma^2}$ and half width at half maximum γ. Area S of one Lorentzian is given by

$$\begin{aligned} S &= (\text{Amplitude})(\text{half width})\pi \\ &= \frac{h_0^2}{4}\gamma\pi. \end{aligned} \tag{B.4}$$

Parseval's theorem is

$$\int_{-\infty}^{\infty} h^2(t)\ dt = \frac{1}{2\pi}\int_{-\infty}^{\infty} |H(\omega)|^2\ d\omega \tag{B.5}$$

Now we consider a case where the oscillator is excited repeatedly every τ second as described in Figure B.2(b). We now realize that both square integral of $h'(t)$ and the Fourier transform $H'(\omega)$ diverges to infinity. However, the mean square of $h'(t)$ defined as

$$\begin{aligned} < V^2 > &\equiv \lim_{X\to\infty} \frac{1}{2X}\int_{-X}^{X} |h'(t)|^2\ dt \\ &= \frac{1}{\tau}\int_{-\infty}^{\infty} |h'(t)|^2\ d\omega \\ &= \frac{h_0^2}{4\gamma\tau} \end{aligned} \tag{B.6}$$

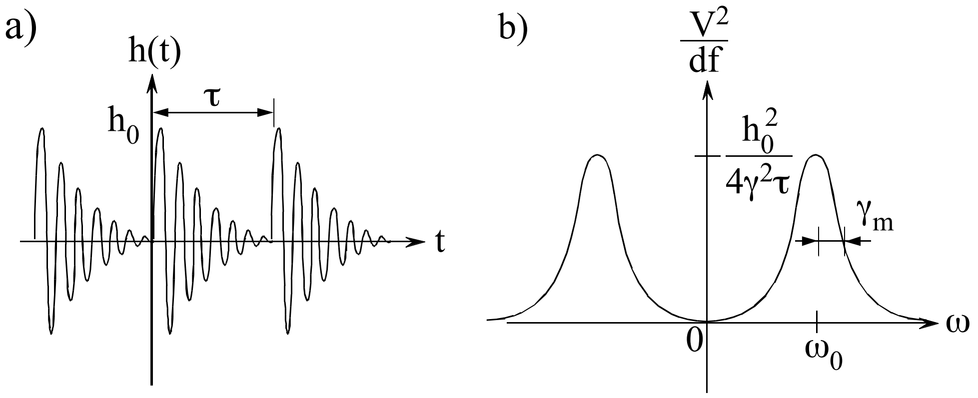

Figure B.2: Signal shape of a periodically excitated damped harmonic oscillator in (a) real time space and (b) frequency space.

is still finite.

This $< V^2 >$ represents power. Power spectral density $\frac{V^2}{df}$ is defined as follows

$$\begin{aligned}\frac{V^2}{df} &\equiv \lim_{X\to\infty} \frac{1}{2X} H'(\omega) H'^*(\omega) \\ &= \frac{1}{\tau}\int_{-\infty}^{\infty} |H(\omega)|^2 \, d\omega \\ &= \frac{2\pi h_0^2}{4\gamma\tau}\end{aligned} \tag{B.7}$$

The plasma mode is thermally excited, which means mode is excited to random amplitude with random duration at random phase. Thermally excited mode signal falls in the power finite signal class and therefore we deal with the power spectral density of the fluctuation, not the energy spectrum.

Appendix C

Transmission line model of the trapped plasma

Wineland and Dehmelt [44] modeled the "trap mode" of a small number of electrons in a harmonic potential using a simple LCR series circuit. Similarly, the collective electron plasma modes in long cylindrical Penning-Malmberg traps have previously been modeled [43] as an extended LCR transmission line, shown in Figure C.1. In this regard, the coupling coefficient $\mathcal{G}$ for an antenna is simply

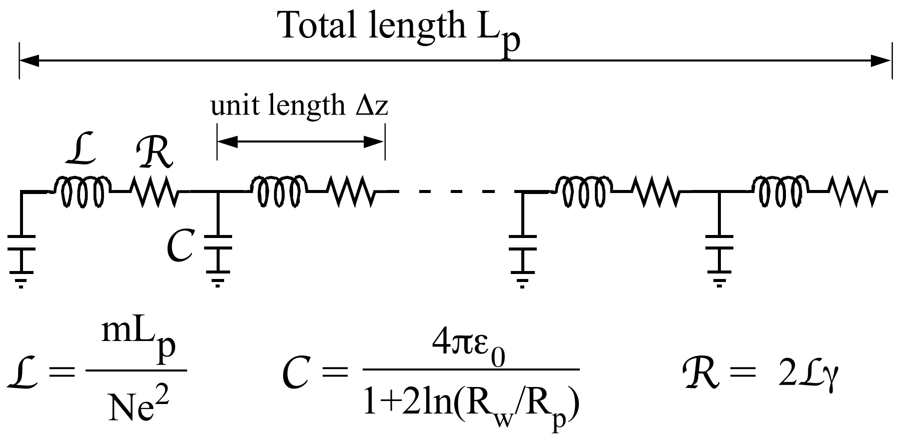

Figure C.1: Transmission line model of plasma in a Penning-Malmberg trap the capacitance between the plasma and the antenna section of the wall, weighted by a "node factor" F_m^2 of the mode. The electrostatic wave propagating through the plasma along the z-axis is analogous to an electromagnetic wave propagating along a coaxial cable. The only difference is that inertia for the plasma wave is provided by the mechanical inertia of the electrons, whereas inertia for the EM wave is provided by the energy being stored in the magnetic field.

The transmission line circuit shown here is described by 3 parameters $\mathcal{L}, \mathcal{C}, \mathcal{R}$, all normalized per unit length Δz, as shown in Figure C.1. $\mathcal{L}$ (the inductance per unit length) represents the inertia of the electron current, and is therefore proportional to m/e for the electron; and it is also inversely proportional to the charge line density eN/L_p. $\mathcal{C}_p$ (the capacitance along z axis per unit length) represents the ratio of electric field induced and displaced charge along axis. $\mathcal{C}$ (the capacitance between the cylindrical wall and the plasma) represents how much voltage is induced on the wall when charge is present in the plasma. $\mathcal{R}$ (the resistance per unit length) represents the damping of a mode.

Overall, this simple model gives expressions of $v_\phi, \mathcal{G}$ as:

$$\begin{aligned} v_\phi \equiv \frac{\omega_m}{k_m} &= \frac{1}{\sqrt{\mathcal{L}\mathcal{C}}} \\ &= \omega_p R_p \left[\frac{1}{2} + \frac{1}{2}\ln\frac{R_w}{R_p}\right]^{1/2}, \end{aligned} \tag{C.1}$$

$$\mathcal{G} = \mathcal{C} L_p F_m^2. \tag{C.2}$$

The finite length L_p discretizes the modes at $k_m = m_z\pi/L_p$. The sinusoidal mode factor F_m enters squared because impedances Z representing voltage over current inherently involve transmission and reception. Eq. (C.1) is analogous to Eq.(3.1), with $T = 0$ and $R_w \gg R_p$. One can reproduce Eq.(3.1) by adding a thermal pressure term [6] in the calculation of $\mathcal{L}$.

Appendix D

Noise Measurement of Modes

This Appendix D presents a set of calculations and discussions developed by prof. R.W. Gould. It served as a conceptual basis for the experiment. These (unpublished) notes are included here for completeness and for present and future referenceability.

D.1 Part I

For noise purposes, the plasma can be represented by a noise voltage source V_s in series with its internal impedance Z_s (Thevenin) or, alternatively, a noise current source I_s in parallel with its internal admittance, Y_s (Norton), as shown in Figure D.1. Y_s is just the reciprocal of Z_s. These two approaches are equivalent and will give the *same* results, but one may be preferable than the other, depending on circuit details. In this case, the Norton equivalent seems preferable because several of the circuit elements appear in parallel and *parallel admittances simply add*. According to Nyquists theorem the mean square open-circuit noise voltage per unit bandwidth df, is $V_s^2/df = 4kTRe\{Z_s\}$, and the mean square short-circuit noise current per unit bandwidth df, is $I_s^2/df = 4kTRe\{Y_s\}$.

In [21] it was shown theoretically that the plasma admittance, as would be measured at a sector probe when the frequency is *close to that of one of the resonant modes*, would be of the form

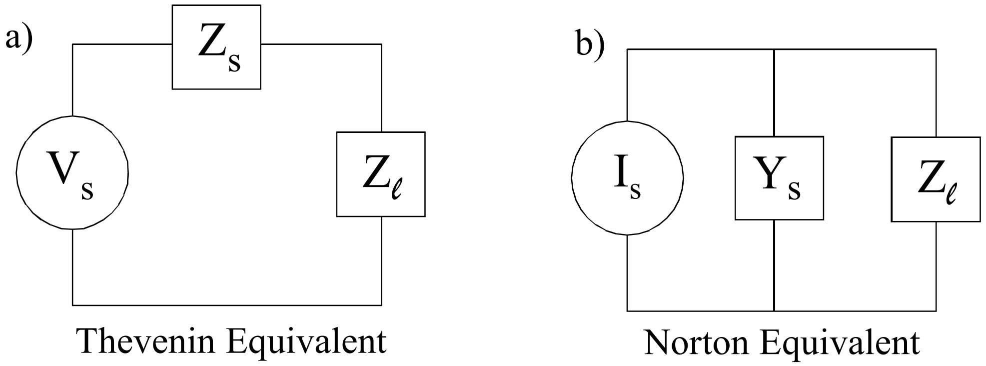

Figure D.1: (a) Thevenin and (b) Norton equivalent circuit.

$$Y_s \equiv \frac{1}{Z_s} \approx \frac{R_m}{j(\omega - \omega_m) + \gamma_m} + jB_c \tag{D.1}$$

where ω_m is the resonant frequency of *one* of the many modes, γ_m is the damping rate of that mode, R_m is the residue at this simple pole (related to a coupling factor), and B_c comes from a sum over all the nonresonant mode and represents a sector *capacitance*. From physical arguments one would expect a pole at the frequency of each mode because at that frequency only a tiny voltage applied to the sector is required to produce a large induced charge (or current) on the sector. Since a measurement cannot be made at the sector itself, we include the capacitance of the cable from the sector to the point at which the measurement can be made (at the flange). This cable capacitance appears in *parallel* with Y_s so it appears as additive term in Eq. (D.1). Hence it *just increases the value of* B_c. Note that we are using the electrical engineering convention, $exp(j\omega t)$ rather than the physics convention $exp(-i\omega t)$. In Fig. D.2 we show a discrete component representation of the admittance of Eq. (D.1), together with the parallel cable capacitance and a "load" which represents the input admittance of the noise-measuring preamplifier: its input resistance in parallel with a small stray capacitance. The LRC circuit on the left gives the simple pole in the admittance Y_s.

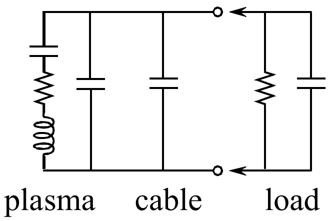

Figure D.2: Component representation of Eq.(D.1), with cable and load.

We will use this expected form of the admittance function to discuss the measurement results. Hopefully, the measurements will be consistent with this form, and be able to determine values for the various parameters. To reduce the number of parameters needed we will *normalize all admittances* to the characteristic admittance ($Y_o = 1/Z_o = 1/50\Omega = .02\mho$) of the transmission line on which directional coupler measurements of the plasma admittance is based, and use lower case letters to denote these normallized admittances. We also introduce a new frequency variable $x = (\omega - \omega_m)\omega_m$ which is zero at the mode center, a new *dimensionless* damping parameter $\epsilon = \gamma_m/\omega_m$, and a new *dimensionless* residue parameter $\rho = R_m/\omega_m Y_o$, so that Eq. (D.1) can be rewritten as

$$y_s = \frac{\rho}{jx + \epsilon} + j\ b_c \tag{D.2}$$

Typically $\rho \sim .001, b_c \sim .25(200pf\ at\ 4Mhz)$ and ϵ, the mode damping, varies with temperature from .0001 or less to about .01. We note that and $\epsilon = \rho$ and $x = 0$, corresponds to the plasma impedance of 50Ω at resonance, were it not for the cable capacitance. We also note that we could still reduce the number of parameters by one more if we were to divide x and ρ by ϵ. However, in the experiment, the mode damping is an important parameter, and we don't want to obscure that parameter.

Finally the *complex reflection coeffecient* of this admittance, as measured with a 50Ω directional coupler is

$$r = \frac{1 - y_s}{1 + y_s} \tag{D.3}$$

The inverse of this relation,

$$y_s = \frac{1 - r}{1 + r} \tag{D.4}$$

is needed to convert measurements of the complex reflection coefficient to an admittance.

Eqs. (D.1)-(D.4) are examples of bilinear transformations (see any book on complex variables). For example, if we think of x as a *complex* frequency variable, although mostly we are interested in real values of x, then Eq. (D.2) maps a point in the complex x plane to another point in the complex y_s plane. It also maps curves in the complex x plane into curves in the complex y_s plane. *Circles in the x plane are mapped in to in the y_s plane.* A straight line, such as the real x axis, is a special case of a circle which has infinite radius. Frequencies in the upper half x plane correspond to damped disturbances, poles in the upper half plane to damped (stable) modes, and the upper half x plane maps into the *interiorof the unit circle* in the complex r plane.

In Figure D.3(a), we show how the real x axis maps into the complex y_s plane for three different values of damping $\epsilon = .0003, .001$, and $.003$ with $\rho = .001$ and $b_c = .25$.

The bilinear transformation Eq. (D.3) maps the circles of Figure D.3(a) into the circles of Figure D.3(b) in the complex reflection coefficient plane, all within the unit circle. In both sets of plots, frequency is a parameter, going from 10 half-linewidths below resonance to 10 half-linewidths above resonance. As the frequency increases from below resonance to above resonance, curves are traced out in a *clockwise* direction (using the $exp(j\omega t)$ convention). In the complex y_s plane the curves asymptote to jb_s far from resonance. The middle circle, in both plots, is for $\epsilon = .001 (\epsilon = \rho)$. This corresponds to a mode damping such that plasma admittance is very nearly equal to $1/50\Omega$ at resonance. The outer circles, in both plots, are for

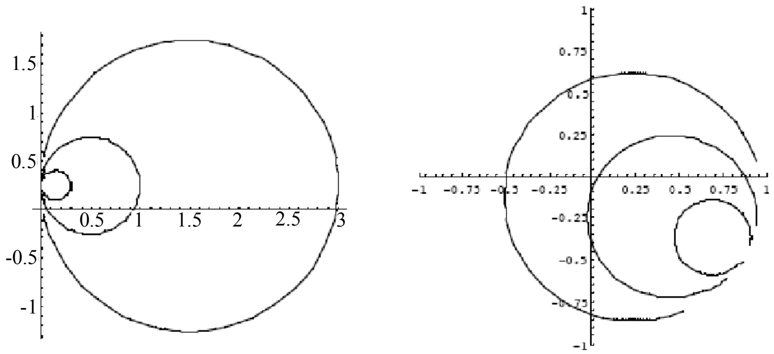

Complex y_s plane.
(ε=0.0003 - outermost circle)

Complex r plane.
(ε=0.0003 - outermost circle)

Figure D.3: (a)Complex y_s plot and (b)Complex r plot.

lower temperature (narrower linewidth) and higher plasma admittance, whereas the inner circles are for higher temperature (broader linewidth) and lower plasma admittance. In the complex r plane the curves asymptote to $(1 - jb_s)/(1 + b_s)$ far from resonance. We have chose to plot the in the complex admittance plane with frequency as a parameter, but the real and imaginary parts of y_s versus frequency are contained implicitly in these maps and we show them explicitly in Figures D.4(a) and D.4(b), respectively.

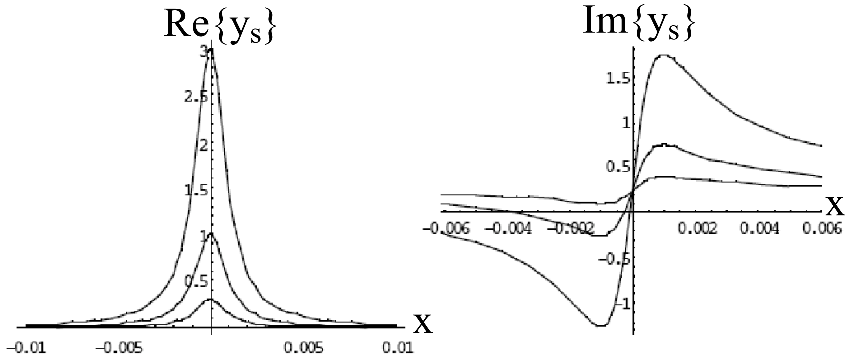

Figure D.4: (a) Real and (b) Imaginary part of y_s versus x.

Since the measurement of r will be a measurement of its magnitude and phase we show in Figure D.5 what these are expected to look like using this model. This is just a different way of looking at the information presented in Figure D.3(b) and it is straightforward to go from one display to the other. In Figure D.5(a), the case with heaviest damping ($\epsilon = .003$) has the smallest "dip" and in Fig D.5(b), the smallest phase variation. The lightly damped case ($\epsilon = .0003$) has the biggest phase variation (2π when one accounts for the artificial discontinuity) because in Figure D.3(b), the curve encircles the origin. The asymptotic phase, far from resonance, is $2 * Atan(b_c) \sim 28°$. In the absence of the sector and cable capacitance, this would be zero, and the plots of Fig. 5ab would be symmetric and antisymetic aboutthe center frequency.

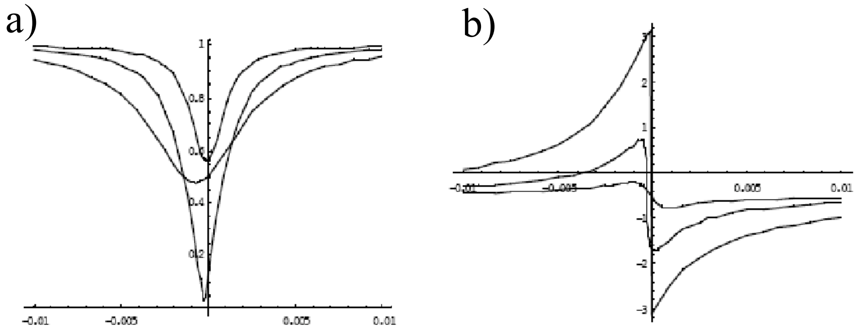

Figure D.5: (a) Magnitude and (b) Phase of r versus x.

We note that any error in measuring the phase (which should be *zero with an open circuit*) has the effect of *rotating* the curves in Figure D.3(b) about the origin by an angle equal to the phase error. In turn, this changes the admittance map (and therefore the real and imaginary parts of the admittance), although a rotated circle in Figure D.3(b) still transforms to a circle (another circle) in Figure D.3(a).

The mean square noise current per unit bandwidth in the Norton equivalent circuit is, according to the Nyquist theorem, equal to $4kTY_oRe\{y_s\}(Y_o = .02mho)$ and so should look like Figure D.4(a). This is the current which would flow if the

y_ℓ were a *short circuit* ($y_\ell = \infty$).

However, the noise measuring circuit preamplifier has an input admittance: $y_\ell = .05 + jb_\ell$ (1000Ω resistor in parallel with some small *stray* capacitance). The noise current flows through the preamplifier input admittance measuring circuit and generates the noise voltage which is observed by the measurement circuit. To get this noise voltage, we take the noise current to flow into the *parallel combination* of y_s and y_ℓ which is just the sum of y_s and y_ℓ. Thus

$$v^2_{meas}/df = \frac{4kT}{Y_o}\frac{Re\{y_s\}}{|y_s + y_\ell|^2} \tag{D.5}$$

When $y_\ell = 0$ (amplifier has infinite input impedance) this expression just gives the Thevenin result for the open circuit noise voltage because $Y_o Re\{y_s\}/|y_s|^2$ is just $Re\{Z_s\}$. Thus the effect of adding the load is to reduce v^2_{meas}/df by a factor

$$F = \left|\frac{y_s}{y_s + y_\ell}\right|^2 \to 1, \text{when } y_\ell = 0, \tag{D.6}$$

from that which would appear across the cable capacitance alone. F is plotted versus frequency in Figure D.6. The minima occur because y_s passes close to zero on the low side of resonance (see Figure D.3(a)). The deepest curve is for a lightly damped mode ($\epsilon = .0003$). This effect is strongly dependent on the value of cable capacitance.

Suggested measurement proceedure.

Directional coupler measurement of admittance. a) with the input to the directional coupler *open*, adjust the reference phase of the lock-in so that the phase of the reflection is zero. Placing a short at the input of the directional coupler should change that phase to 180°. In both cases the magnitude of the reflection coefficient should be unity. Replacing the short at the input by a 50Ω termination should give a reflection coefficient of zero, with a phase which is undefined. Of course, small errors in the directional coupler and/or termination may not give precisely zero for the reflection coefficient. b) From the measurement of the complex reflection coefficient, the complex admittance (or its reciprocal the

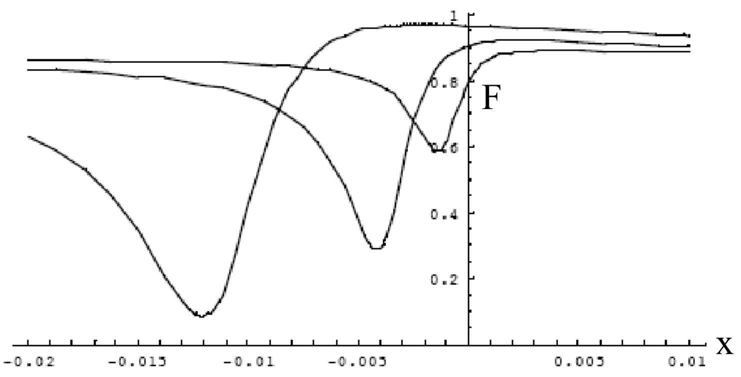

Figure D.6: Plot of F versus x.

complex impedance) can be calculated from Eq. (D.4). It is probably useful to plot the r and y_s obtained this way in the complex plane, as well as a plots of there real and imaginary parts versus frequency.

Noise measurement. Measure the mean square noise voltage (per unit frequency interval) v^2_{meas}/df, versus frequency.

Temperature determination. At this point there are several ways one could proceed. Refering to Eq. (D.5), it would be useful to plot both v^2_{meas}/df and $Re\{y_s\}/|y_s + y_\ell|^2$ versus frequency. According to Eq. (D.5), they should be proportional differing by a factor $4kT/Y_o$. If they are then the temperature is easily determined. There are bound to be some differences, hopefully only minor. Then one might determine the temperature from the peak value of the noise emission, provided that it is close to the peak value of $Re\{y_s\}/|y_s + y_\ell|^2$.

A suggestion: The cable and sector capacitances complicate the data analysis and interpretation somewhat. Since the measurements are made over a rather narrow band of frequencies, this capacitive admittance can be cancelled by placing an inductor in parallel with the cable. For example, at 4 MHz a 7.9μ inductance cancels $200pf$ cable capacitance. This cancelation is *much* broader than the rather narrow line widths, and probably also than the shifts in mode frequency produced by changes in plasma temperature. This has the added advantage of increasing the sensitivity since the input impedance of the preamp (1k) becomes the load, rather than the cable capacitance, about 5 times higher. The main penalty is that the inductance should be changed if the frequency is changed more that 10-20%. Note, Sateesh Pillai used this trick in studying the resistive destabilization of the $m = 2$ diocotron mode. Since the $m = 1$ diocotron mode has a substantially different frequency one probably doesn't have to worry about its destabilization. If the inductive cancelation scheme seems to be of interest, I can provide you with figures similar to those above, with $b_c = 0$, and a little interpretation.

D.2 Part II

Will external loading cool a mode? We know that a mode is, in general, damped so that when a mode is excited the mode energy W_m decays according to

$$\frac{dW_m}{dt} = -2\gamma_m W_m. \tag{D.7}$$

where γ_m is the linear decay constant of the mode. In the case of thermal excitation the mode energy is $W_m = kT_m$. However, we do not expect the energy of a *thermally* excited mode to decay, rather the decay is *balancedby continuous excitation* by random processes to give the thermal equilibrium fluctuation level of the mode. This can be accounted for by adding another term to Eq. (D.7),

$$\frac{dT_m}{dt} = -2\gamma_m (T_m - T_p) \tag{D.8}$$

where T_p is the plasma temperature and T_m is the "mode" temperature, and we have substituted $W_m = kT_m$. In steady state $dT_m/dt = 0$ and the mode temperature is equal to the plasma temperature. If somehow we manage to temporarily increase or decrease the mode temperature, this equation says that it will return to the plasma temperature in a time $1/(2\gamma_m)$.

When there is additional mode damping by some process *external* to the plasma, such as damping due to an external load, it is convenient to describe that additional damping by an additional damping constant, γ_ℓ. If the external load has a temperature T_ℓ different from the plasma temperature, then it will also be a source (or sink) of thermal energy for the mode. This can be modeled by adding still another term to Eq. (D.8)

$$\frac{dT_m}{dt} = -2\gamma_m (T_m - T_p) - 2\gamma_\ell (T_m - T_\ell). \tag{D.9}$$

So we have the plasma trying to drive the mode to temperature T_p and the load trying to drive the mode to temperature T_ℓ. The linear decay time of the mode consists of the internal part plus the external part and is just the sum of the two contributions, $\gamma_m + \gamma_\ell$. In the steady state $dT_m/dt = 0$, and the mode temperature is somewhere and between T_p and T_ℓ

$$T_m = \frac{\gamma_m T_p + \gamma_\ell T_\ell}{\gamma_m + \gamma_\ell} \tag{D.10}$$

If the additional contribution to the mode damping due to the load is much smaller than that due to the plasma, $\gamma_\ell \ll \gamma_p$, then T_m will be very close to to the plasma temperature, T_p. Conversely, if the external damping dominates, then T_m will be close to the load temperature. In this discussion we have assumed that cooling one mode of the plasma, does not significantly affect the plasma temperature because of the very large number of modes and particles ($> 10^7$).

In order for a measurement of the fluctuation level of a mode to give an accurate measure of plasma temperature, the external contribution to mode damping should be small. Alternatively, one could correct for the load contribution to temperature using Eq. (D.10) if one knows γ_m, γ_ℓ, and T_ℓ.

Now, let's examine the experimental situation more specifically. Near a mode resonance, the plasma admittance has the form

$$Y_s \approx \frac{R_m}{j(\omega - \omega_m) + \gamma_m} + jB_c \tag{D.11}$$

This suggests an equivalent circuit for the noise measurement shown in Figure D.7(a), and its equivalent, Figure D.7(b):

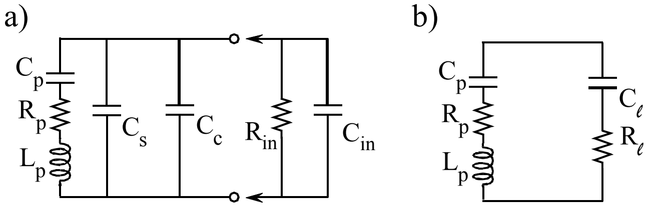

Figure D.7: (a) Equivalent circuit for noise measurement and (b) its equivalent circuit.

For purposes of discussion, we have combined the three parallel capacitances (C_s the sector capacitance, C_c the cable capacitance, and C_{in} the preamp input capacitance) into a single capacitance, $C_s + C_c + C_{in}$ (which is dominated by the cable capacitance). We then expressed this parallel capacitance and parallel input resistance, R_{in}, of the preamp as a *series* circuit, R_ℓ and C_ℓ, as shown in Figure D.7(b). We see immediately that C_ℓ appears in series with C_p and this *reduces* the capacitance of the resonant circuit slightly (since $C_\ell \gg C_p$) and therefore *shifts the mode frequency slightly upward.* We also see that R_ℓ appears in series with R_p and this increases the resistance so that *damping of the mode is increased.*

One can also see that so that $\gamma_\ell/\gamma_p = R_\ell/R_p$ so that the additional fractional damping is just equal to the additional fractional resistance which the load adds. According the earlier argument, we should make this small to minimize the error in the temperature determination. To estimate this,

$$R_\ell = Re\left\{\frac{1}{\frac{1}{R_{in}} + j\omega C_{in}}\right\} = \frac{R_{in}}{1 + \omega^2 C^2 R_{in}^2} \approx \frac{1}{\omega^2 C^2 R_{in}} \tag{D.12}$$

since R_{in} ($\sim 1k\Omega$ to $10k\Omega$) and $1/\omega C \sim 300\Omega$. Thus R_ℓ is in the range 90Ω to 9Ω. Clearly the larger the input resistance of the preamp, the less mode damping the preamp introduces, and therefore the smaller the error in temperature. Since R_p is 50Ω, and higher for higher plasma temperature, a preamp input resistance of $10k\Omega$ or greater is desireable.

It is rather hard to estimate T_ℓ, the load temperature, since it may involve not only some resistance at room temperature, but possibly some contribution from the noise of the first stage of the preamp, normally higher than room temperature unless it is cooled.

Bibliography

[1] M. Amoretti, C. Amsler, G. Bonomi, et al. Production and detection of cold antihydrogen atoms. *Nature*, 419:456, 2002.

[2] M. Amoretti, C. Amsler, G. Bonomi, et al. Positron plasma diagnostics and temperature control for antihydrogen production. *Phys. Rev. Lett.*, 91:55001, 2003.

[3] F. Anderegg, E.M. Hollmann, and C.F. Driscoll. Rotating field confinement of pure electron plasmas using trivelpiece-gould modes. *Phys. Rev. Lett.*, 81:4875, 1998.

[4] G. Bekefi. *Radiation Processes in Plasmas*. John Wiley and sons, Inc., New York, 1966. §8.4.

[5] D.C. Champeney. *Fourier Transforms and their Physical Applications*. Academic Press, New York, 1973.

[6] F.F. Chen. *Introduction to Plasma Physics*. Plenum Press, New York, 1974.

[7] R.C. Davidson. *Physics of Nonneutral Plasmas*. Addison-Wesley, 1990. §5.5.2.

[8] C.F. Driscoll, J.H. Malmberg, and K.S. Fine. Observation of transport to thermal equilibrium in pure electron plasmas. *Phys. Rev. Lett.*, 60:1290, 1988.

[9] D.H.E. Dubin. Theory of electrostatic fluid modes in a cold spheroidal nonneutral plasma. *Phys. Rev. Lett.*, 66:2076, 1991.

[10] D.H.E. Dubin. personal note, 2001. unpublished.

[11] D.H.E. Dubin and T.M. O'Neil. Cross-magnetic field heat conduction in nonneutral plasmas. *Phys. Rev. Lett.*, 78:3868, 1997.

[12] D.H.E. Dubin and T.M. O'Neil. Trapped nonneutral plasmas, liquids, and crystals (the thermal equilibrium states. *Reviews of Modern Physics*, 71:87, 1999.

[13] D.L. Eggleston, C.F. Driscoll, B.R. Beck, A.W. Hyatt, and J.H. Malmberg. Parallel energy analyzer for pure electron plasma devices. *Phys. Fluids B*, 4:3432, 1992.

[14] J.V. Evans and M. Loewenthal. Ionospheric backscatter observations. *Planetary Space Sci.*, 12:915, 1964.

[15] I. Fidone, G. Giruzzi, and G. Taylor. Plasma diagnostics in the tokamak fusion test reactor using emission of electron cyclotron radiation at arbitrary frequencies. *Phys. Plasmas*, 3:2331, 1996.

[16] L.R. Fortney. *Principles of electronics : analog and digital*. Harcourt Brace Jovanovich, San Diego, 1987.

[17] D.E. Fray. *American Institute of Physics Handbook*. McGraw-Hill, New York, 1963. §5.

[18] G. Gabrielse, N.S. Bowden, P. Oxley, et al. Driven production of cold antihydrigen and the first measured distribution of antihydrogen states. *Phys. Rev. Lett.*, 89:213401, 2002.

[19] A. Gillespie and F. Raab. Thermally excited vibrations of the mirrors of laser interferometer gravitational-wave detectors. *Phys. Rev. D*, 52:577, 1995.

[20] R.W. Gould. Dynamics of non-neutral plasmas. *Phys. Plasmas*, 2:2151, 1995.

[21] R.W. Gould. Thermal excitation of modes in a non-neutral plasma. In F. Anderegg, L. Schweikhard, and C.F. Driscoll, editors, *Non-Neutral Plasma Physics IV*, pages 263–270, New York, 2002. American Institute of Physics.

[22] R.G. Greaves and C.M. Surko. Antimatter plasmas and antihydrogen. *Phys. Plasmas*, 4:1528, 1997.

[23] Hewlett-Packard. *Application Note 150*, 1989.

[24] E.M. Hollman. *Experimental Studies of Cross-Magnetic-Field Transport in Nonneutral Plasm*
PhD thesis, University of California at San Diego, 1999.

[25] E.M. Hollmann, F. Anderegg, and C.F. Driscoll. Measurement of cross-magnetic-field heat transport in a nonneutral plasma. *Phys. Rev. Lett.*, 82:4839, 1999.

[26] E.M. Hollmann, F. Anderegg, and C.F. Driscoll. Confinement and manipulation of non-neutral plasmas using rotating wall electric fields. *Phys. Plasmas*, 7:2776, 2000.

[27] A.W. Hyatt. *Measurement of the Anisotropic Temperature Relaxation Rate in a Magnetized*
PhD thesis, University of California at San Diego, 1988.

[28] A.W. Hyatt, C.F. Driscoll, and J.H. Malmberg. Measurement of the amisotropic temperature relaxation rate in a pure electron plasma. *Phys. Rev. Lett.*, 59:2975, 1987.

[29] J.K. Jennings, R.L. Spencer, and K. C. Hansen. Numerical calculation of axisymmetric electrostatic modes for cold finite-length non-neutral plasmas. *Phys. Plasmas*, 2:2630, 1995.

[30] C. Kittel. *Elementary statistical physics*. Wiley, New York, 1958.

[31] K.H. Knoll, G. Marx, K. Hubner, F. Schweikert, S. Stahl, C. Weber, and G. Werth. Experimental g_j factor in the metastable $5d_{3/2}$ level of Ba^+. *Phys. Rev. A*, 54:1199, 1996.

[32] N. Meyer-Vernet and C. Perche. Tool kit for antennae and thermal noise near the plasma frequency. *J. Geophys. Res.*, 94:2405, 1989.

[33] T.B. Mitchell, J.J. Bollinger, D.H.E. Dubin, X.-P. Huang, W.M. Itano, and R.H. Baughman. Direct observations of structural phase transitions in planar crystallized ion plasmas. *Science*, 282:1290, 1998.

[34] N.T. Nakata, G.W. Hart, and B.G. Peterson. Using the plasma noise spectrum to measure the parallel temperature in a nonneutral plasma. In F. Anderegg, L. Schweikhard, and C.F. Driscoll, editors, *Non-Neutral Plasma Physics IV*, pages 271–276, New York, 2002. American Institute of Physics.

[35] S. Nunomura, D. Sansonov, and J. Goree. Transverse waves in a two-dimensional screened-coulomb crystal (dusty plasma). *Phys. Rev. Lett.*, 84:5141, 2000.

[36] H. Nyquist. Thermal agitation of electric charge in conductors. *Phys. Rev.*, 32:110, 1928.

[37] T.M. O'Neil and D.H.E. Dubin. Thermal equilibria and thermodynamics of trapped plasmas with a single sign of charge. *Phys. Plasmas*, 5:2163, 1998.

[38] S.A. Prasad and T.M. O'Neil. Waves in a cold pure electron plasma of finite length. *Phys. Fluids*, 26:665, 1983.

[39] S.A. Prasad and T.M.O'Neil. Finite length thermal equilibria of a pure electron plasma column. *Phys. Fluids*, 22:278, 1979.

[40] R.L. Stenzel and R.W. Gould. Upper-hybrid resonance absorbtion, emission, and heating of an afterglow plasma column. *J. Appl. Phys.*, 42:4225, 1971.

[41] J.P. Sullivan, S.J. Gilbert, and C.M. Surko. Excitation of molecular vibrations by positron impact. *Phys. Rev. Lett.*, 86:1494, 2001.

[42] T.M.O'Neil and C. F. Driscoll. Transport to thermal equilibrium of a pure electron plasma. *Phys. Fluids*, 22:266, 1979.

[43] A.W. Trivelpiece and R.W. Gould. Space charge waves in cylindrical plasma columns. *J. Appl. Phys.*, 30:1784, 1959.

[44] D.J. Wineland and H.G. Dehmelt. Principles of the stores ion calorimeter. *J. Appl. Phys.*, 46:919, 1975.